Magnetic Induction Systems to Harvest Energy from Mechanical Vibrations

by

Aparna S Jonnalagadda

Submitted to the Department of Mechanical Engineering
in partial fulfillment of the requirements for the degree of

Master of Science in Mechanical Engineering

at the

MASSACHUSETTS INSTITUTE OF TECHNOLOGY

February 2007

Author ....
Department of Mechanical Engineering
January 26, 2007

Certified by ....
Alexander H Slocum
Professor of Mechanical Engineering
Thesis Supervisor

Certified by ....
Jeffrey H Lang
Professor of Electrical Engineering and Computer Science
Thesis Supervisor

Accepted by ....
Lallit Anand
Chairman, Department Committee on Graduate Students

Magnetic Induction Systems to Harvest Energy from Mechanical Vibrations

by

Aparna S Jonnalagadda

Submitted to the Department of Mechanical Engineering
on January 26, 2007, in partial fulfillment of the
requirements for the degree of
Master of Science in Mechanical Engineering

Abstract

This thesis documents the design process for magnetic induction systems to harvest energy from mechanical vibrations. Two styles of magnetic induction systems – magnet-through-coil and magnet-across-coils – were analyzed. MATLAB models were created to serve as a design aid and optimization tool for both styles of magnetic induction systems. Prototypes were built to test the predictions of the MATLAB models. The experimental data was found to be in good agreement with the model predictions.

Thesis Supervisor: Alexander H Slocum
Title: Professor of Mechanical Engineering

Thesis Supervisor: Jeffrey H Lang
Title: Professor of Electrical Engineering and Computer Science

Acknowledgments

I am extremely grateful to my advisor, Professor Alex Slocum, for his academic guidance and personal support over the past few years. I would like to declare my particular gratitude to him for introducing me to the joy of nailguns and plasma cutters. I am equally indebted to Professor Jeff Lang for all his help, and especially for his patient encouragement during my struggle with magnetic induction equations. I am truly lucky to have had the good fortune of working with two wonderful supervisors who took a personal interest in my growth and well-being.

I am thankful to Toru Takagi for his support during all phases of the project, and for the generous loan of his car and driving time to collect vibration data. I am grateful to my labmates Zac Trimble and Keith Durand for their help with day-to-day work on my thesis. I would also like to thank Maureen Lynch for handling all the administrative details cheerfully and supercompetently.

Gerry Wentworth, Mark Belanger, David Breslau, Tony Caloggero and Andrew Carvey deserve special thanks for their help with the machining and assembly of parts for my thesis in the Laboratory for Manufacturing & Productivity and the Edgerton Student Shop. I would like to thank Kayla Jacobs for her encouragement and her help with proof-reading my thesis drafts.

Finally, this thesis could not have been completed without the unwavering love and support of my family. Alex Rolfe put totally ridiculous amounts of time and effort into keeping me fed, focused and motivated. My parents and extended family, though too far away to contribute in the same way, have given me invaluable moral support and strength at all times.

Contents

List of Figures

List of Tables

Chapter 1

Introduction

The global rise of energy consumption has highlighted the need to develop and implement novel methods of harvesting, conserving, and optimally utilizing energy. Mechanical vibrations are a commonly over-looked and sadly under-utilized source of renewable energy. The unwanted vibrations produced by the operation of mechanical devices – lawn-mowers, cars, air compressors – are just one example of the multitude of untapped energy sources in everyday life. Developing methods to harvest energy from these vibrations is a particularly exciting challenge because of the large number of potential applications for these methods. Furthermore, harvesting energy from undesirable vibrations would reduce noise in the vibrating systems. The goal of this thesis is to create models to serve as a design aid and optimization tool for systems that harvest energy from mechanical vibrations.

Vibration in automobiles provides an excellent case-study to the explore the feasibility of energy harvesting from vibrating surfaces. Power windows and locks on car doors in present-day cars require connection to the main battery. Providing connections to the power windows (and power locks) between the car battery and all the doors of the car requires an elaborate wiring harness, increasing the complexity of the car design and adding significantly to the car weight and cost. In addition, the wiring to the car doors often succumbs to the stress imposed by opening and closing the car doors, leading to reliability concerns. The centralized wiring system makes car repair difficult because the wires are hard to access.

A solution to these inconveniences would be 'wireless' car doors, where each door is a separate module that snaps on to the main car frame to build a complete car. This would greatly simplify the wiring harness and reduce its weight and cost. Malfunctioning or damaged doors could be replaced in a matter of minutes by simply switching in a different module.

The major challenge in this approach is providing power to the windows and the door locks without connecting them to the car battery. One way of achieving this would be to have a separate battery in every door, but current battery technology does not provide options with suitable weight, cost and lifespan to make this feasible. An alternative would be to design a system to harvest and store energy from car vibrations, and use this energy to power the windows and locks. This would make every door completely self-sufficient and enable the 'wireless door' concept to be implemented successfully.

The focus of this thesis is to prove the feasibility of such a system and document the creation of a proof-of-concept prototype. Chapter 2 details the energy requirements for car windows and defines the required energy harvesting system output. It also presents a brief survey of possible energy harvesting techniques, and magnetic induction is selected as the most promising candidate for further investigation. Following this, Chapter 3 covers the theory of magnetic induction as applicable for two embodiments of the process. This theory forms the basis of MATLAB models that predict the energy harvesting capability of a magnetic induction systems as a function of the system geometry and the properties of the magnets and coils used. Chapter 4 discusses the equations and design considerations of a complete energy harvesting system. The predictions made by the MATLAB models are presented in the next chapter. Chapter 6 documents the tests conducted to verify the model predictions. The concluding chapter discusses the implications of the experimental results and makes recommendations for future work to build on this thesis.

Chapter 2

Energy Harvesting

Energy harvesting can be implemented in many ways. Determining the energy requirements of an application is essential for the selection of an appropriate energy harvesting stategy. This chapter discusses the energy requirements of the car window system and the selection of an energy harvesting strategy to meet these specifications.

2.1 Energy Requirements

Identifying the energy requirements of a system is the first step towards determining whether energy harvesting is a feasible approach to satisfy them. The energy requirements of the car windows are specified in terms of a power budget. The power budgets for current car windows and new efficient windows are given in Tables 2.1 and 2.2 respectively[1].

The current window designs are mechanically inefficient and require approximately 510 joules per open-close cycle. The new efficient window design will bring down the energy requirement per open-close cycle to approximately 160 joules. Assuming one window open-close cycle every five minutes as a conservative estimate, the power requirement for current car windows is 1.7 watts, and the requirement for new efficient windows is approximately 0.53 watts.

2.2 Energy Harvesting Strategies

There are many ways of harvesting energy from vibrations. Three of the most common methods are : Variable Capacitance Systems, Piezoelectric Material Systems, and Magnetic

---

[1] Keith Durand, MIT SM Thesis, June 2007

Description	Value	Units
Weight of moving components	27	N
Travel	0.5	m
Drag force	70	N
Counterbalance	15	N
Travel time (each way)	4.0	s
Motor efficiency	55	%
Gear efficiency	50	%
Mechanism efficiency	50	%
Current (raise) @ 13.6 VDC	5.5	A
Current (lower) @ 13.6 VDC	3.9	A
Energy to raise	300	J
Energy to lower	210	J
Total Energy per cycle	510	J

Table 2.1: Power budget for current car window mechanisms

Description	Value	Units
Weight of moving components	32	N
Travel	0.5	m
Drag force	70	N
Counterbalance	50	N
Travel time (each way)	4.0	s
Motor efficiency	70	%
Gear efficiency	80	%
Mechanism efficiency	80	%
Current (raise) @ 13.6 VDC	1.1	A
Current (lower) @ 13.6 VDC	1.8	A
Energy to raise	60	J
Energy to lower	100	J
Total Energy per cycle	160	J

Table 2.2: Power budget for new efficient window mechanisms

Induction Systems. Each of these will be explained and their typical power outputs evaluated. Table 2.3 shows a comparison table of the three options.

2.2.1 Variable Capacitance Systems

Variable capacitance systems employ parallel-plate capacitors with movable plates. The plates are charged to a specified voltage. The plates are then mechanically moved apart by the input vibrations. Increasing the distance between the plates causes energy to be stored in the capacitor. This energy can be harvested when the plates are brought closer to each other again. The magnitude of energy that can be harvested from such systems is generally on the order of microwatts[2,3].

2.2.2 Piezoelectric Material Systems

Piezoelectric materials build up a voltage differential across their ends when they are subjected to mechanical deformation. When energy from vibrations is harnessed to cause deformation in such materials, the voltage difference generated can be used to charge a capacitor or other energy-storage device. The magnitude of energy harvested from piezoelectric systems can vary from microwatts[4] to watts[5].

2.2.3 Magnetic Induction Systems

Magnetic induction systems generate power through relative motion between a coil of wire and a magnet. This causes the magnetic flux through the coil to change, which leads the generation of a voltage differential across the ends of the wire coil. This voltage difference can be used to charge a capacitor or other energy-storage device. The magnitude of energy harvested from magnetic induction systems can range up to kilowatts[6] depending on the size of the system. The comparison table (Table 2.3) shows this to be the most cost-effective and promising option for powering car windows.

---

[2] Bernard Chih-Hsun Yen, MIT SM Thesis, February 2005

[3] José Oscar Mur Miranda, MIT PhD Thesis, February 2004

[4] Rajendra K Sood, MIT SM Thesis, September 2003

[5] Onnik Yaglioglu, MIT SM Thesis, January 2002

[6] Sivananda Kumjula Reddy, MIT SM Thesis, June 2005

	Variable Capacitance	Piezo Material	Magnetic Induction
Power generation	μW	μW-W	mW-kW
Vibration amplitude	μm	μm	mm-cm
Driving frequency	Any range	Tens of Hz	Any range
Ease of system design	Difficult	Easy	Easy
Cost	High	High	Modest
Lifetime	Low	High	High

Table 2.3: Comparison of energy harvesting strategies.

2.3 Summary

This chapter presented the power generation target of 0.5 watts for the energy harvesting system. Magnetic induction systems were chosen for further investigation because of their high energy density for low cost compared to piezoelectric material or variable capacitance systems. The next chapter is devoted to the detailed analysis of two types of magnetic induction systems, magnet-through-coil and magnet-across-coils, and the selection of the magnet-across-coils system to implement the energy harvesting system.

Chapter 3

Magnetic Induction System Design

The power that can be harvested by a magnetic induction system depends on many factors, including the size and geometric configuration, the magnetic flux density of the magnets, the number of turns of wire in the coil, and the excitation frequency. This chapter presents the equations that govern two styles of magnetic induction systems – magnet-through-coil and magnet-across-coils – in order to enable an understanding of how these systems can be designed and optimized for specific applications.

The aim of analyzing these magnetic induction systems is to calculate their output voltage and power, which are the parameters of interest for the design of an energy harvesting system. The first step in the process is to calculate the magnetic field, H, in the system. The magnetic field dictates the magnitude of magnetic flux density, B, and hence the magnetic flux, λ, through the coils. Once the flux through the coils is known, the open-circuit voltage across them, V, can be calculated using Faraday's Law. Ohm's Law and Kirchhoff's Laws are then used to determine the average power, P, dissipated through a load resistor attached to the system. Figure 3-1 shows a flowchart of the steps involved in the analysis of magnetic induction systems.

3.1 Magnet-through-coil Induction

This section describes the governing equations for voltage generation by a magnet translating through a coil with no relative rotation. The advantage of this kind of magnetic induction system is that it is easy to build; the disadvantage is that the coil never experiences a complete flux reversal, and thus the voltage and power generated is low.

A common example of this type of system is a shaker flashlight. The flashlight is powered

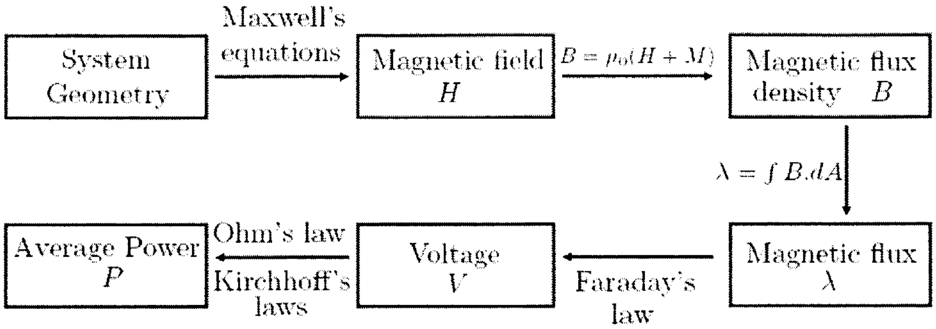

Figure 3-1: Flowchart of steps in magnetic induction system analysis.

not by batteries but by the motion of a magnet relative to a coil when the device is shaken.

3.1.1 Geometry

The magnet-through-coil induction system consists of a cylindrical coil that translates relative to a bar magnet of height l_m and radius r_m. The longitudinal axis of the magnet is set along the y-axis, with its midpoint at the origin. The coil, made of N turns of wire, has height l_c, inner diameter d_{min} and outer diameter d_{max}. The average radius of the coil, r_c, is calculated as

$$r_c = \frac{d_{min} + d_{max}}{4}.$$

The average diameter of the coil, d_c, is $2r_c$. The cross sectional area of the coil, A_c, is calculated as

$$A_c = \pi r_c^2.$$

The magnet is fixed in place while the coil moves along the y-axis. The y-coordinate of the lower end of the coil is defined as h. The coil is assumed to vibrate with a fixed amplitude, a, at a single frequency, f, with the motion centered at the y-coordinate d_o. Figure 3-2 shows the labeled geometry of this system and Table 3.1 lists the variables used.

3.1.2 Magnetic flux Generated by the Bar Magnet

The bar magnet is modeled as two point magnetic charges situated at $\pm l_m/2$ on the y-axis. The magnitude of the magnetic point charges, q_m, is obtained by integrating the magnetization, $\mu_0 M$, over the cross-sectional areas of the magnet ends. Thus,

$$q_m = \mu_0 M \pi r_m^2. \tag{3.1}$$

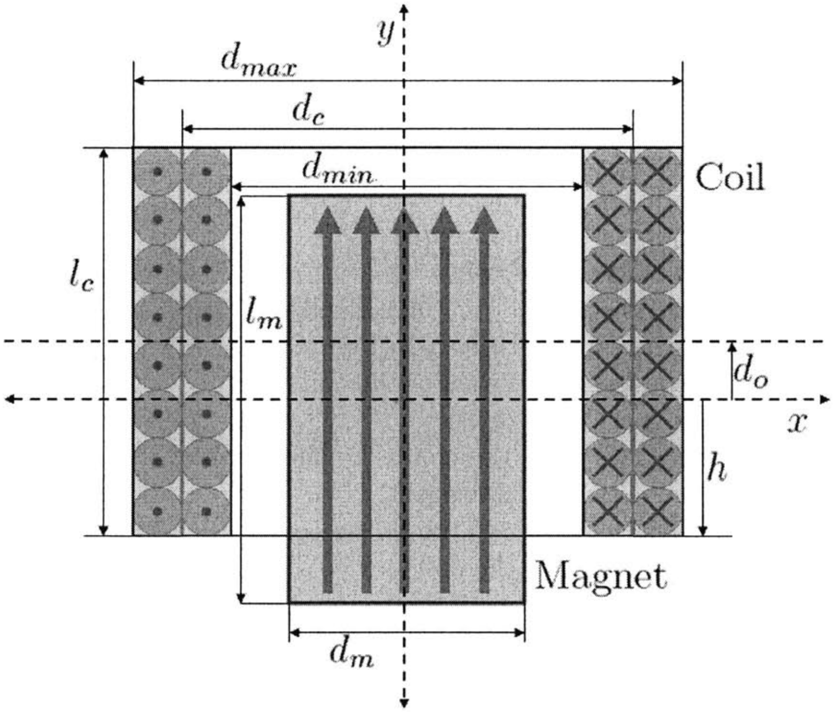

Figure 3-2: A cross-sectional view of the magnet-through-coil induction system. The blue arrows represent the magnetization of the magnet.

Symbol	Units	Variable
a	m	Amplitude of coil vibration
d_c	m	Average diameter of the coil
d_{max}	m	Outer diameter of the coil
d_{min}	m	Inner diameter of the coil
d_o	m	y-coordinate about which vibration is centered
f	Hz	Frequency of coil vibration
h	m	y-coordinate of the lower end of the coil
l_c	m	Height of the coil
l_m	m	Height of the bar magnet
l_w	m	Length of the coil wire
q_m	Wb	Total magnetic flux emanating from a magnetic charge
q_1	Wb	Magnetic charge representing the North Pole of the bar magnet
q_2	Wb	Magnetic charge representing the South Pole of the bar magnet
r_c	m	Average radius of the coil
r_m	m	Radius of the bar magnet
r_w	m	Radius of the coil wire
v	m/s	Velocity of the coil
A_c	m^2	Cross-sectional area of the coil
A_{cap}	m^2	Surface area of the cap (Figure 3-4)
A_w	m^2	Cross-sectional area of the coil wire
B	T	Magnetic flux density
H	m	Distance from the charge to the plane of the coil end
H_m	A/m	Magnetic field strength
I	A	Current flowing through the coil and load resistor
L_c	Wb/A	Inductance of the coil
M	A/m	Magnetization of the magnet
N	$-$	Number of turns of wire in the coil
R	m	Radius of the imaginary sphere around the magnetic charge
R_c	Ω	Resistance of the coil
R_L	Ω	Load resistance across which power is dissipated
V	V	Open-circuit voltage generated across the ends of the coil
V_c	V	Voltage across the coil when a load resistance is attached
V_L	V	Voltage across the load resistor
P	W	Power dissipated through load resistor
μ_0	Tm/A	Magnetic permeability of air
ρ	Ωm	Resistivity of the coil wire material
ϕ_{total}	Wb	Total magnetic flux due to the bar magnet
ϕ_M	Wb	Magnetic flux inside the bar magnet
ϕ_1	Wb	Magnetic flux due to the North Pole of the bar magnet
ϕ_2	Wb	Magnetic flux due to the South Pole of the bar magnet

Table 3.1: Nomenclature for Magnet-through-coil Induction system

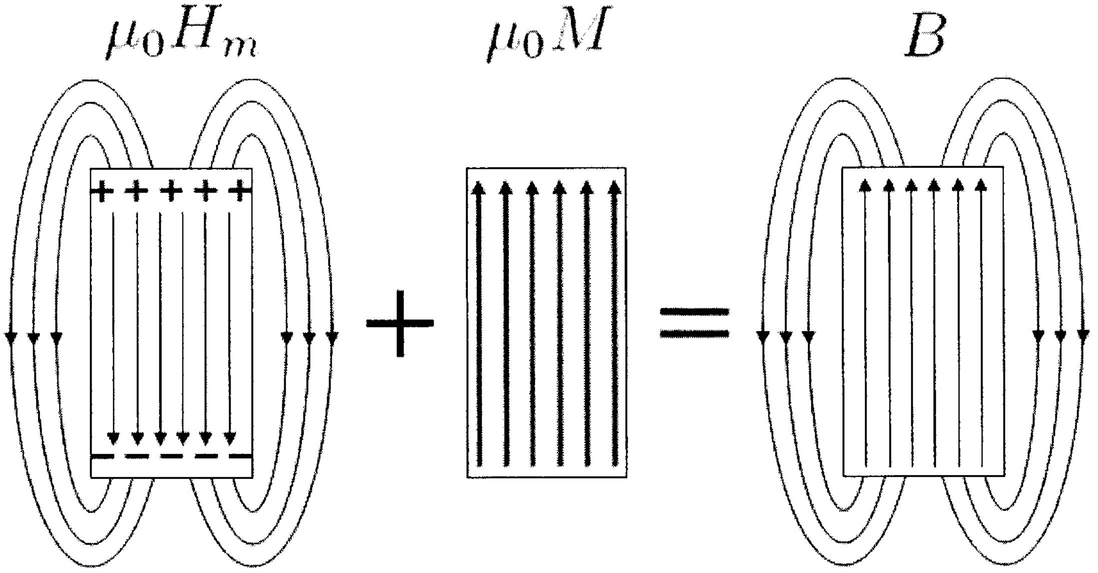

Figure 3-3: Magnetic flux density from a bar magnet.

The magnetic flux density at a given point, B, depends on two terms: the magnetic field strength H_m; and the local magnetization. The local magnetization is M inside the magnet and 0 outside. Figure 3-3 shows how the contributions from these two terms add up to the magnetic flux density:

$$B = \mu_0(H_m + M). \tag{3.2}$$

As shown in Figure 3-3, a bar magnet has a uniform magnetic charge density on its ends at $x = \pm l_m/2$. We make the simplifying assumption that the bar magnet can be modeled as two point magnetic charges located on the y-axis at $\pm l_m/2$. Thus, while the $\mu_0 M$ term we calculate is exact, the $\mu_0 H$ term is an approximation because it comes from a point-charge assumption. We will concentrate on the calculation of $\mu_0 H_m$ and then add it to the simple $\mu_0 M$ term towards the end to arrive at B inside the magnet. Outside the magnet the $B = \mu_0 H$ alone.

The total flux emanating from the magnetic charge is q_m. The resultant flux through any given turn of wire is the fraction of the total flux that passes through the area enclosed by the wire turn; and this flux is numerically equal to the same fraction of q_n. If a sphere is imagined around the point charge, and a single wire turn intersects the sphere to delineate a spherical cap (Figure 3-4), then it follows from Gauss' Law that the magnetic flux through

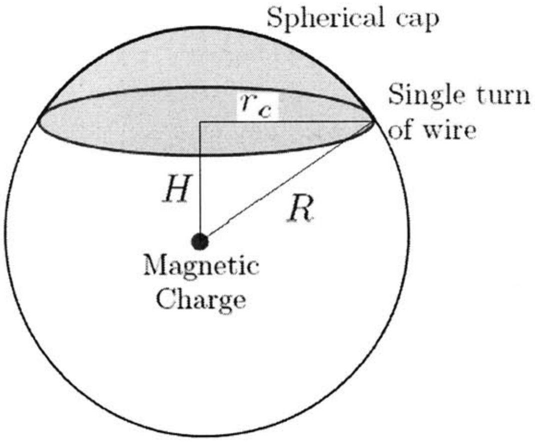

Figure 3-4: Point charge and single wire turn geometry.

the wire turn is equal to the magnetic flux escaping through the cap. Thus, the magnetic flux through the wire turn is proportional to the ratio of the surface area of the cap to the surface area of the entire sphere. For a sphere of radius R, with a distance H from its center to the plane of the coil, the surface area of the cap formed is

$$A_{cap} = 2\pi R(R - H). \tag{3.3}$$

Therefore, the magnetic flux through a single wire turn of radius r_c at a height H above a point charge q_m is given by

$$\phi = q_m \frac{2\pi R(R - H)}{4\pi R^2} = \frac{q_m(R - H)}{2R} = \frac{q_m(\sqrt{r_c^2 + H^2} - H)}{2\sqrt{r_c^2 + H^2}}. \tag{3.4}$$

The magnetic flux through a wire turn in the induction system depends on contributions from the magnetic charges at both ends of the bar magnet. The labeled geometry of the magnetic charges and a single wire turn is shown in Figure 3-5. The magnetic charges have opposite signs to represent the North and South poles of the magnet, with q_1 positive and q_2 negative. In addition, the direction of the magnetic flux through the wire turn changes when a magnetic charge passes from one side of the wire turn to the other. Sign functions are added to Equation 3.4 to account for these changes in the magnetic flux directions. The

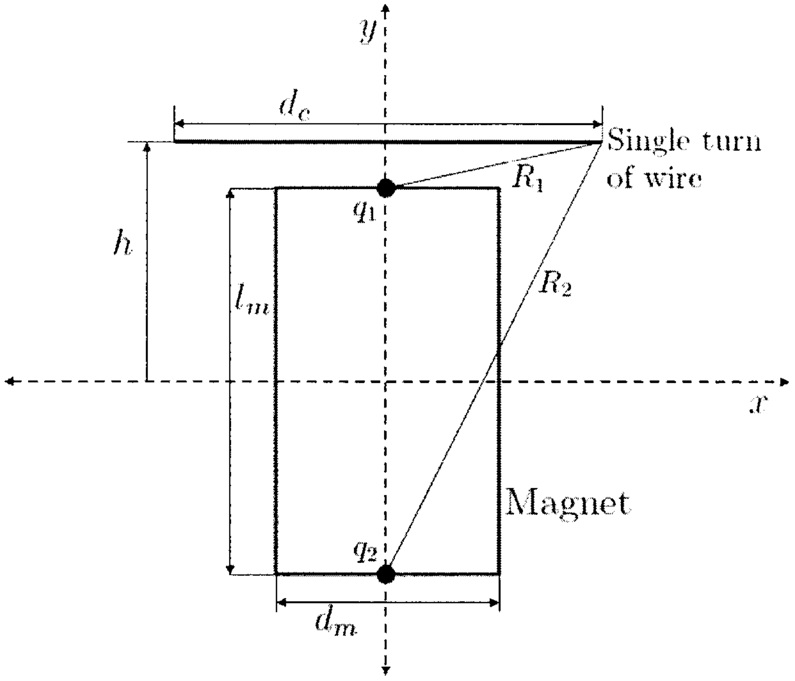

Figure 3-5: Magnetic dipole and single wire turn geometry.

magnetic flux contributions $\phi 1$ and $\phi 2$ from the magnetic charges q_1 and q_2 respectively are

$$\phi_1 = \operatorname{sign}(h - \frac{l_m}{2})\frac{-q_m(\sqrt{r_c^2 + (h - \frac{l_m}{2})^2} - |h - \frac{l_m}{2}|)}{2\sqrt{r_c^2 + (h - \frac{l_m}{2})^2}}, \tag{3.5}$$

$$\phi_2 = \operatorname{sign}(h + \frac{l_m}{2})\frac{q_m(\sqrt{r_c^2 + (h + \frac{l_m}{2})^2} - |h + \frac{l_m}{2}|)}{2\sqrt{r_c^2 + (h + \frac{l_m}{2})^2}}. \tag{3.6}$$

ϕ_1 and ϕ_2 are the fluxes from the point charges at the ends of the bar magnet; when they are divided by the area of the wire turn, they sum up to the $\mu_0 H_m$ component of B. In addition, there is magnetic flux inside the bar magnet due to its magnetization; the magnitude of this flux is $\mu_0 M \pi r_m^2$, which from Equation 3.1 is equal to q_m. Therefore the flux due to $\mu_0 M$ term can be expressed as:

$$\phi_M = \begin{cases} q_m & -l_m/2 < y < l_m/2. \\ 0 & y < -l_m/2 \cup l_m/2 < y. \end{cases} \tag{3.7}$$

The total magnetic flux through a single wire turn at height h is the sum of ϕ_1, ϕ_2 and ϕ_M from Equations 3.5, 3.6 and 3.7 respectively. This sum is multiplied by the number of turns of wire per unit height, N/l_c, and a small incremental height, dy, to obtain the magnetic flux through all the wires coiled at height h. The total magnetic flux through the coil of length l_c is the integral of the magnetic flux over the height of the coil:

$$\phi_{total} = \int_{h}^{h+l_c} \frac{N(\phi_1 + \phi_2 + \phi_M)}{l_c} dy. \tag{3.8}$$

3.1.3 Coil Inductance and Resistance

The inductance of the coil, L_c, is a function of the number of turns, cross-sectional area, and height of the coil. The inductance for a long thin coil, where $l_c > sqrt(A_c)$, is given by:

$$L_c = \frac{\mu_0 N^2 A_c}{l_c} = \frac{\mu_0 \pi N^2 r_c^2}{l_c}. \tag{3.9}$$

The resistance of the coil, R_c, depends on the resistivity of the wire material, ρ, the length of the coiled wire, l_w, and the cross-sectional area of the wire, A_w. If the radius of the wire is r_w, we have

$$l_w = N\pi d_c,$$

$$A_w = \pi r_w^2,$$

$$R_c = \frac{\rho l_w}{A_w} = \frac{\rho(N 2\pi r_c)}{(\pi r_w^2)} = \frac{2N\rho r_c}{r_w^2}. \tag{3.10}$$

If $R_c \gg 2\pi f L_c$, the effects of the system inductance are negligible in comparison to those of the system resistance. Since this relation often holds true in real systems, the subsequent analysis assumes that the resistance effects dominate the system.

3.1.4 Voltage and Power Generation

Faraday's Law states that the open-circuit voltage induced across a turn of wire is the negative integral of the time-change in magnetic flux over the cross-sectional area of the turn. By the chain rule of differentiation, the time-change in magnetic flux can be separated into two multiplicative terms – the change in magnetic flux over height, and the change in coil height over time (in other words, the velocity of the coil). Thus,

$$V = \int \frac{d\phi_{total}}{dt} dA = \int \frac{d\phi_{total}}{dh} \frac{dh}{dt} dA. \tag{3.11}$$

The formula for $\frac{d\phi_{total}}{dh}$ can be calculated by differentiating Equation 3.8 to arrive at

$$\frac{d\phi_{total}}{dh} = \frac{d}{dh}\int_{h}^{h+l_c} \frac{N(\phi_1+\phi_2)}{l_c} dh = \frac{N(\phi_1+\phi_2)}{l_c}\Big|_{h}^{h+l_c}. \tag{3.12}$$

Given the velocity of the coil, v, the open-circuit voltage induced across the coil can be calculated:

$$V = \int \frac{vN(\phi_1+\phi_2)}{l_c}\Big|_{h}^{h+l_c} dA. \tag{3.13}$$

P is the power delivered by the system to a load, modeled here as a resistor R_l. Since the system inductance is assumed to be negligible, the open-circuit voltage generated across the ends of the coil is now applied across the resistances R_c and R_L in series. Then, Kirchoff's Voltage Law implies that

$$V = V_c + V_L, \tag{3.14}$$

where V_c and V_L are the voltages across the coil and load resistor respectively. I is the resultant current flowing through the circuit. Ohm's Law states that the voltage across a resistor is the product of the resistance and the current flowing through it; applying this to Equation 3.14 allows us to solve for the value of I:

$$V = I(R_c + R_L).$$

$$\Rightarrow I = \frac{V}{(R_c + R_L)}. \tag{3.15}$$

The instantaneous power dissipated across the load resistance is the product of the current flowing through it and the voltage across it. This gives

$$P = V_L I = (R_L I^2),$$

and substituting the value for I from Equation 3.15,

$$P = \frac{R_L V^2}{(R_c + R_L)^2}. \tag{3.16}$$

Since R_L is fixed, we differentiate P with respect to R_L to find the maximum:

$$\frac{dP}{dR_L} = \frac{d}{dR_L}\frac{R_L V^2}{(R_c + R_L)^2} = 0.$$

$$\Rightarrow \frac{V^2}{(R_c + R_L)^2} - \frac{2R_L V^2}{(R_c + R_L)^3} = 0. \Rightarrow (R_c + R_L) - 2R_L = 0.$$

$$\Rightarrow R_L = R_c. \tag{3.17}$$

Hence, the load resistance should be matched to the coil resistance in order to extract the maximum possible power from the system.

3.2 Magnet-across-coils Induction

This section describes the governing equations for voltage generation by a magnet moving across coils. This kind of magnetic induction system is more complicated to build; however, the coils experience complete flux reversals, and thus the voltage generated is high. The frequency of flux reversals can be further increased by using multiple N-S magnet pairs.

3.2.1 Geometry

The magnets-across-coils induction system consists of a layer of magnets separated by an air gap from a layer of coils. The magnets move across the coils, causing a change in magnetic flux and generating a voltage across the coil ends. The system has three phases: A, B and C. Figure 3-6 shows a schematic of the system to be analyzed and Table 3.2 lists the variables in the system.

Since the permeability of a magnetic material like steel is typically orders of magnitude higher than that of air, the magnetic backing for the coils and magnets is assumed to have infinite permeability. The now simplified problem is to solve for the magnetic fields in the gap between the two layers of magnetically permeable material, where magnetic fields are generated by the magnets and by coil current.

As all the elements of the system are linear, the fields due to the magnets and coils can each be calculated separately and then added by superposition. This breaks the problem into three smaller tasks: (1) calculation of the magnetic field due to the magnets; (2) calculation of the fields due to the flow of current in the coils; and (3) adding them by superposition and finding the total voltage and power generated.

3.2.2 Magnetic Field Generated by the Magnets

Within the system with magnets, there are two regions: Region A, between $x = 0$ and $x = x_A$, with the magnets; and Region B, between $x = 0$ and $x = -x_B$, with the air gap and

Symbol	Units	Variable
$2d$	m	Gap between adjacent magnets
$2g$	m	Length of a coil phase in the z direction
i_A	A	Current passing through phase A coil
i_B	A	Current passing through phase B coil
i_C	A	Current passing through phase C coil
l	m	Length of a magnet in the z direction
n	$-$	Number of magnetic poles in the system
t	m	Gap between adjacent coils
w	m	Width of a magnet
x_A	m	x-coordinate of the magnet-steel interface
x_B	m	x-coordinate of the coil-steel interface
A_A	m^2	Cross-sectional area bounded phase A coil
A_B	m^2	Cross-sectional area bounded phase B coil
A_C	m^2	Cross-sectional area bounded phase C coil
A_w	m^2	Cross-sectional area of the wire used for coils
B_x	Wb/m^2	Magnetic flux density in the x-direction
B_z	Wb/m^2	Magnetic flux density in the z-direction
H_{A_x}	A/m	Magnetic field in the x-direction in region A
H_{B_x}	A/m	Magnetic field in the x-direction in region B
H_{A_z}	A/m	Magnetic field in the z-direction in region A
H_{B_z}	A/m	Magnetic field in the z-direction in region B
L	Wb/A	Self-Inductance of a coil
M	Wb/A	Mutual Inductance between different phase coils
N	$-$	Number of turns of wire in a coil
P_A	W	Power dissipated through load resistor across phase A coil
P_B	W	Power dissipated through load resistor across phase B coil
P_C	W	Power dissipated through load resistor across phase C coil
R	Ω	Resistance of each coil phase
R_L	Ω	Load resistance on each phase for power dissipation
V_A	V	Voltage across phase A coil
V_B	V	Voltage across phase B coil
V_C	V	Voltage across phase C coil
λ_A	Wb	Magnetic flux through phase A coil
λ_B	Wb	Magnetic flux through phase B coil
λ_C	Wb	Magnetic flux through phase C coil
μ_0	Tm/A	Magnetic permeability of air; $4\pi \times 10^{-7}$
$\psi_{(coils)}$	A	Scalar Magnetic potential due to coils
$\psi_{A(magnets)}$	A	Scalar Magnetic potential in Region A due to magnets
$\psi_{B(magnets)}$	A	Scalar Magnetic potential in Region B due to magnets
σ_M	T	Magnetic charge density at the interface between magnets and air
ω	rad/s	Operating frequency of the system

Table 3.2: Nomenclature for Magnet-across-coils Induction system

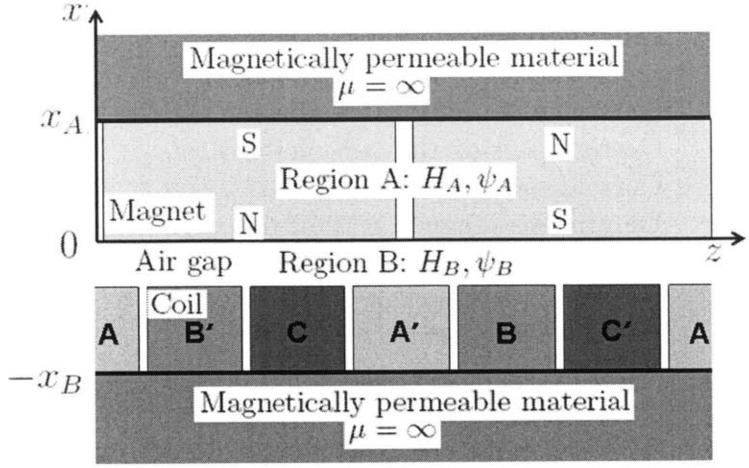

Figure 3-6: Magnet-across-coils induction system.

coils. These regions have distinct magnetic fields, H_A and H_B respectively. The interface between the magnetic region and the air gap provides the boundary conditions on the fields in these two regions. The x-axis is defined such that $x = 0$ at the interface between the magnets and air.

The magnetic charge is concentrated on the planes at the ends of the magnets at $x = 0$. The magnetic charge density on the z-axis is represented by $\sigma_M(z)$. Figure 3-7 shows a schematic of the magnet placement and the resulting graph of $\sigma_M(z)$ as a function of z.

The charge density function from Figure 3-7 can be represented by a Fourier series. Then we can solve for the magnetic field caused by a sine wave charge distribution, and use superposition to get the total field.

The charge density waveform can be represented by

$$\sigma_M = a_{0(\sigma_M)} + \sum_{k=1}^{\infty}[a_{k(\sigma_M)}\cos(\frac{2\pi kz}{Z}) + b_{k(\sigma_M)}\sin(\frac{2\pi kz}{Z})], \tag{3.18}$$

where Z is the spatial period of the magnetic charge density function and the Fourier coefficients are:

$$a_{0(\sigma_M)} = 0. \tag{3.19}$$

$$a_{k(\sigma_M)} = 0. \tag{3.20}$$

$$b_{k(\sigma_M)} = \begin{cases} \frac{4\sigma_{max}}{k\pi}\cos\left(\frac{\pi kd}{l+2d}\right) & \text{for odd } k. \\ 0 & \text{for even } k. \end{cases} \tag{3.21}$$

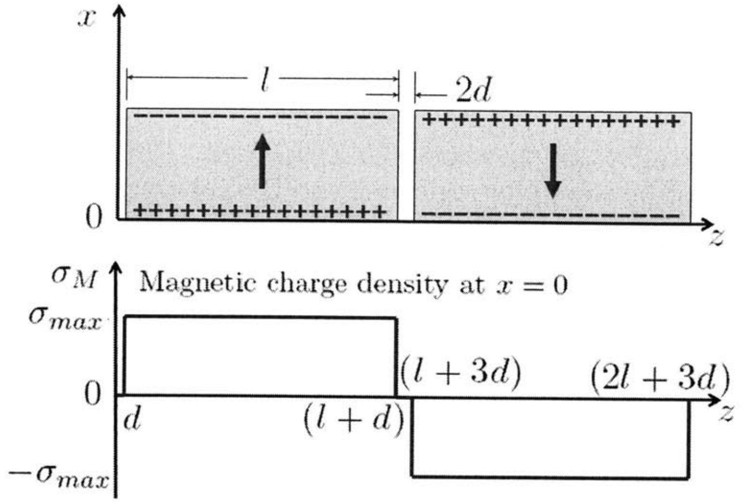

Figure 3-7: Schematic of the magnet placement and the resulting charge density on the z-axis.

The details of the Fourier coefficient calculations can be found in Section 1 of Appendix C.

Since the magnetic charge density waveform is reducible to a sum of sines, we solve for the magnetic fields resulting from a sinusoidal charge density ($\sigma_{M_k} = b_{k(\sigma_M)} \sin(\frac{2\pi kz}{Z})$) on the z-axis. For a system with current J, Maxwell's Equations state that:

$$\nabla \times H = J. \tag{3.22}$$

$$\nabla \cdot B = 0. \tag{3.23}$$

Since we are solving the part of the superposition that only considers the fields due to the magnets, there is no current in the system and J in Equation 3.22 is zero. This means that the curl of H is zero, which implies that H is the negative gradient of some scalar magnetic potential function ψ.

$$\begin{aligned} &\nabla \times H = 0. \\ &\Rightarrow H = -\nabla \psi. \end{aligned} \tag{3.24}$$

From Equations 3.2, 3.23 and 3.24, we get

$$\nabla \cdot \mu(-\nabla \psi + M) = 0. \tag{3.25}$$

Because the magnetization M of a magnet is a constant, and M of air is zero, in both cases $\nabla \cdot M$ vanishes. Thus we get the simplified equation

$$\nabla^2 \psi = 0. \tag{3.26}$$

This equation must be solved for regions A and B to obtain the corresponding magnetic potentials (ψ_A and ψ_B) in those regions. To satisfy Equation 3.26, the solutions must be of the form

$$\psi_A = [\alpha_1 \sin(\frac{2\pi kz}{Z}) + \alpha_2 \cos(\frac{2\pi kz}{Z})] \times [\alpha_3 \sinh(\frac{2\pi kx}{Z}) + \alpha_4 \cosh(\frac{2\pi kx}{Z})].$$

$$\psi_B = [\beta_1 \sin(\frac{2\pi kz}{Z}) + \beta_2 \cos(\frac{2\pi kz}{Z})] \times [\beta_3 \sinh(\frac{2\pi kx}{Z}) + \beta_4 \cosh(\frac{2\pi kx}{Z})].$$

The values of the constants in these equations are obtained by applying the boundary conditions on the regions. The first two boundary conditions arise at the interfaces with the magnetically permeable backings at $x = x_A$ and $x = -x_B$. Given the absence of surface currents at these interfaces, the tangential magnetic field, H_z is conserved. We have assumed that the materials have $\mu = \infty$; therefore $B = \mu H$ dictates that $H = 0$ in order for B to be finite. Since $H = 0$, the tangential field H_z must be zero at these interfaces. The interface between the magnets and air at $x = 0$ is considered next. The conservation of the tangential magnetic field, H_z, (given the absence of surface currents at $x = 0$), and the conservation of the normal magnetic flux, B_x, yield two more boundary conditions for the system. In conclusion, the boundary conditions applicable are :

1. $H_{A_z} = 0$ at $x = x_A$.
2. $H_{B_z} = 0$ at $x = -x_B$.
3. $H_{A_z} = H_{B_z}$ at $x = 0$.
4. $\mu_0 H_{A_x} + b_{k(\sigma_M)} \sin(\frac{2\pi kz}{Z}) = \mu_0 H_{B_x}$ at $x = 0$.

Solving for the values of the constants is now a matter of algebraic manipulation. Boundary conditions (1) and (2) state that H_{A_z} and H_{B_z} are zero-valued at x_A and $-x_B$ respectively. H_{A_z} and H_{B_z} are the partial derivatives of $-\psi_A$ and $-\psi_B$ with respect to z, so for them to be zero at x_A and $-x_B$ respectively, the x-dependent components of ψ_A and ψ_B must be zero. This means that the x-dependent components of the magnetic potentials must be sinh functions, since cosh functions cannot be zero-valued at any points. This means that the constants $\alpha_2, \alpha_4, \beta_2$ and β_4 are zero. Constants α_1 and α_3 can be combined into α, and β_1 and β_3 into β.

$$\psi_A = \alpha \sin(\frac{2\pi kz}{Z}) \sinh(\frac{2\pi k(x-x_A)}{Z}). \tag{3.27}$$

$$\Rightarrow H_{A_z}\Big|_{x=x_A} = -\frac{2\pi k\alpha}{Z}\cos(\frac{2\pi kz}{Z})\sinh(\frac{2\pi k(x-x_A)}{Z})\Big|_{x=x_A} = 0.$$

$$\psi_B = \beta \sin(\frac{2\pi kz}{Z}) \sinh(\frac{2\pi k(x+x_B)}{Z}). \tag{3.28}$$

$$\Rightarrow H_{B_z}\Big|_{x=-x_B} = -\frac{2\pi k\beta}{Z}\cos(\frac{2\pi kz}{Z})\sinh(\frac{2\pi k(x+x_B)}{Z})\Big|_{x=-x_B} = 0.$$

Now we have two equations (boundary conditions (3) and (4)) and two unknowns (the values of the two constants α and β); the following steps show the rearrangement of variables to arrive at the answer.

$$H_{A_z}\Big|_{x=0} = H_{B_z}\Big|_{x=0}.$$

$$\Rightarrow -\frac{2\pi k\alpha}{Z}\cos(\frac{2\pi kz}{Z})\sinh(-\frac{2\pi kx_A}{Z}) = -\frac{2\pi k\beta}{Z}\cos(\frac{2\pi kz}{Z})\sinh(\frac{2\pi kx_B}{Z}).$$

$$\Rightarrow \alpha\sinh(\frac{-2\pi kx_A}{Z}) = \beta\sinh(\frac{2\pi kx_B}{Z}).$$

$$\mu_0 H_{A_x}\Big|_{x=0} + b_{k(\sigma_M)}\sin(\frac{2\pi kz}{Z}) = \mu_0 H_{B_x}\Big|_{x=0}.$$

$$\Rightarrow -\mu_0\frac{2\pi k\alpha}{Z}\sin(\frac{2\pi kz}{Z})\cosh(\frac{-2\pi kx_A}{Z}) + b_{k(\sigma_M)}\sin(\frac{2\pi kz}{Z}) = -\mu_0\frac{2\pi k\beta}{Z}\sin(\frac{2\pi kz}{Z})\cosh(\frac{2\pi kx_B}{Z}).$$

$$\Rightarrow b_{k(\sigma_M)} = \mu_0\frac{2\pi k\alpha}{Z}\cosh(\frac{2\pi kx_A}{Z}) - \mu_0\frac{2\pi k\beta}{Z}\cosh(\frac{2\pi kx_B}{Z}).$$

$$\alpha = \frac{b_{k(\sigma_M)}\sinh(\frac{2\pi kx_B}{Z})}{\frac{2\pi k\mu_0}{Z}(\sinh(\frac{2\pi kx_A}{Z})\cosh(\frac{2\pi kx_B}{Z}) + \sinh(\frac{2\pi kx_B}{Z})\cosh(\frac{2\pi kx_A}{Z}))}. \tag{3.29}$$

$$\beta = \frac{-b_{k(\sigma_M)}\sinh(\frac{2\pi kx_A}{Z})}{\frac{2\pi k\mu_0}{Z}(\sinh(\frac{2\pi kx_A}{Z})\cosh(\frac{2\pi kx_B}{Z}) + \sinh(\frac{2\pi kx_B}{Z})\cosh(\frac{2\pi kx_A}{Z}))}. \tag{3.30}$$

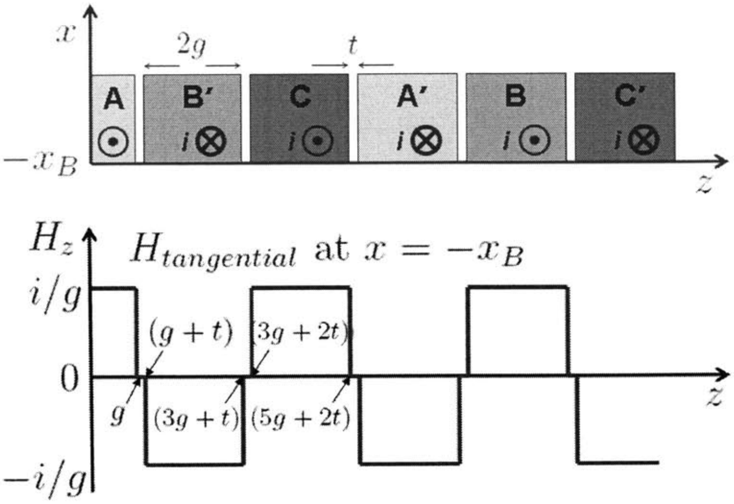

Figure 3-8: Schematic of the coil placement and the tangential magnetic field at $-x_B$ resulting from current i flowing through all three phases of coils.

From equations 3.18, 3.27 and 3.28, the total magnetic potential due to the magnets is :

$$\psi_{A(magnets)} = \sum_{k=1}^{\infty} \alpha \sinh(\frac{2\pi k(x - x_A)}{2(l+2d)}) \sin(\frac{2\pi k z}{2(l+2d)}). \tag{3.31}$$

$$\psi_{B(magnets)} = \sum_{k=1}^{\infty} \beta \sinh(\frac{2\pi k(x + x_B)}{2(l+2d)}) \sin(\frac{2\pi k z}{2(l+2d)}). \tag{3.32}$$

3.2.3 Magnetic Field Generated by Coil Current

For the calculation of the fields due to current flowing through the coils, the magnets are ignored. The current through the coils is approximated as a surface current at $x = -x_B$. This means that there is no difference between Region A and Region B for this calculation. Thus we solve for the magnetic fields from the coils in the region bounded by x_A and $-x_B$. Figure 3-8 shows a graph of the tangential magnetic field H_z at $-x_B$ that would result from a current i flowing through all three phases of coils.

The tangential magnetic field at the surface of the magnetic backing is the sum of the contributions from the three phases A, B and C. The width of each phase is $2g$, and the gap between phases is t. Since the three phases are symmetric, we can solve for one phase and then use superposition to add in the effects from the other two phases. In particular, we will solve for the contribution from current i flowing through the phase A coils. The tangential magnetic field, H_z, at plane $x = -x_B$, due to the current i passing through the phase A coils, can be expressed as

$$H_z = a_{0(H_z)} + \sum_{k=1}^{\infty}[a_{k(H_z)}\cos(\frac{2\pi kz}{Z}) + b_{k(H_z)}\sin(\frac{2\pi kz}{Z})], \tag{3.33}$$

where Z, the spatial period of the tangential magnetic field function, is $6(2g+t)$, and the Fourier coefficients are

$$a_{0(H_z)} = 0, \tag{3.34}$$

$$a_{k(H_z)} = \begin{cases} \frac{4i}{gk\pi}\sin\left(\frac{\pi kg}{3(2t+g)}\right) & \text{for odd } k. \\ 0 & \text{for even } k. \end{cases}, \tag{3.35}$$

$$b_{k(H_z)} = 0. \tag{3.36}$$

The details of the Fourier coefficient calculations can be found in Section 2 of Appendix C.

Since H_z can be expressed as a sum of cosines, we can solve for the contribution from a single harmonic ($H_{z_k} = a_{k(H_z)}\cos(\frac{2\pi kz}{Z})$) and then use superposition to obtain the complete solution. Similarly to the case of the magnets, the boundary conditions on the magnetic field due to coil current are:

1. $H_z = 0$ at $x = x_A$.
2. $H_z = a_{k(H_z)}\cos(\frac{2\pi kz}{6(2g+t)})$ at $x = -x_B$.

Within the region, similar to the case with the magnets,

$$\nabla \times H = 0 \Rightarrow H = -\nabla\psi \Rightarrow \nabla^2\psi = 0.$$

The solution of this equation is the magnetic potential (ψ) due to the current in the coils, and must be of the form

$$\psi = [D_1\sin(\frac{2\pi kz}{Z}) + D_2\cos(\frac{2\pi kz}{Z})] \times [D_3\sinh(\frac{2\pi kx}{Z}) + D_4\cosh(\frac{2\pi kx}{Z})].$$

Since boundary condition (1) states that H_z must be zero at x_A, the x-dependent component of the magnetic potential must be a sinh function.

$$\psi = D\sin(\frac{2\pi kz}{Z})\sinh(\frac{2\pi k(x-x_A)}{Z}).$$

$$\Rightarrow H_z\Big|_{x=x_A} = -\frac{2\pi kD}{Z}\cos(\frac{2\pi kz}{Z})\sinh(\frac{2\pi k(x-x_A)}{Z})\Big|_{x=x_A} = 0.$$

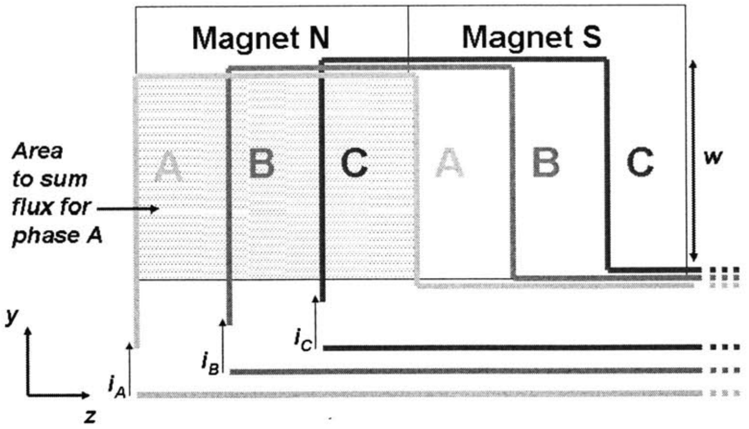

Figure 3-9: Three-phase coil arrangement geometry.

From boundary condition (2), H_z is $a_{k(H_z)}\cos(\frac{2\pi kz}{Z})$ at $-x_B$.

$$H_z\Big|_{x=-x_B} = -\frac{2\pi kD}{Z}\cos(\frac{2\pi kz}{Z})\sinh(\frac{2\pi k(x-x_A)}{Z})\Big|_{x=-x_B} = a_{k(H_z)}\cos(\frac{2\pi kz}{Z}).$$

$$D = \frac{a_{k(H_z)}Z}{2\pi k\sinh(\frac{2\pi k(x_A+x_B)}{Z})}. \tag{3.37}$$

$$\psi_{coils} = \sum_{k=1}^{\infty} D\sinh(\frac{2\pi k(x-x_A)}{6(2g+t)})\sin(\frac{2\pi kz}{6(2g+t)}). \tag{3.38}$$

3.2.4 Coil Self-Inductance, Mutual Inductance, and Resistance

Equation 3.38 allows us to calculate the magnetic potential created by the flow of current through the coils; the magnetic flux density generated can be obtained from this magnetic potential.

$$B_{coils} = \mu_0 H_{coils} = -\mu_0\nabla\psi_{coils}.$$

The magnetic fluxes through the coils due to current through them are $\lambda_{c(A)}, \lambda_{c(B)}$ and $\lambda_{c(C)}$ through phase A, B and C respectively, and can be calculated by multiplying the magnetic flux density and the area of the coils. Figure 3-9 shows the geometry of the three phases. For example, the magnetic flux through phase A coils is:

$$\lambda_{c(A)} = B_{coils}\cdot A_A,$$

where A_A is the area of the phase A coils. Since the coils lie in the $x = -x_B$ plane, only the x-component of the magnetic flux density will pass through them; hence $B_{coils} \cdot A_A = B_{x(coils)} A_A$.

The self-inductance, L, of a coil is defined as the magnetic flux generated through the coil due to the flow of a unit current through it. The mutual inductance between a pair of coils, M, is defined as the magnetic flux generated through one coil due to the flow of a unit current through the other. The magnetic flux through each phase is influenced by the current flowing through every phase. Since everything is symmetric across phases, the self-inductance of each phase and the mutual inductance between each pair of phases is the same. Equation 3.39 defines the dependence of the magnetic fluxes and the current through the coils.

$$\begin{bmatrix} \lambda_{c(A)} \\ \lambda_{c(B)} \\ \lambda_{c(C)} \end{bmatrix} = \begin{bmatrix} L & -M & -M \\ -M & L & -M \\ -M & -M & L \end{bmatrix} \begin{bmatrix} i_A \\ i_B \\ i_C \end{bmatrix} \tag{3.39}$$

To calculate the value of L and M, we consider the flux linked by a phase A coil and a phase B coil due to a current i flowing through the phase A coil (when i_B and i_C are 0):

$$\lambda_{c(A)} = B_{x(coils)} A_A = nN \int_{-l/2}^{l/2} \mu_0 H_{x(coils)} w dz = Li.$$

$$\lambda_{c(B)} = B_{x(coils)} A_B = nN \int_{(2g+t-l/2)}^{(2g+t+l/2)} \mu_0 H_{x(coils)} w dz = -Mi.$$

The integrals are the flux through one coil and one turn of wire; to get the total flux they are multiplied by the number of coils (which should be the same as the number of magnetic poles, n), and the number of turns of wire (N) in each coil. The turns of wire in the coil are approximated into a pointwise lumped distribution; therefore we just multiply by the number of wire turns instead of integrating over the physical width of the turns ($2g$ for each phase). Rearranging the terms, we get:

$$L = \frac{nN}{i} \int_{-l/2}^{l/2} \mu_0 H_{x(coils)} w dz. \tag{3.40}$$

$$M = \frac{nN}{i} \int_{-l/2}^{l/2} \mu_0 H_{x(coils)} w dz. \tag{3.41}$$

Since $H_{x(coils)}$ as a function of i can be calculated from Equation 3.38, the values of L and M can be found.

The resistance of all the coil phases should be the same since they are the same pattern displaced in space. The resistance of each phase depends on the resistivity of the wire material, ρ_w, the cross-sectional area of the wire, A_w, and the total length of the wire, l_w. The length of wire used will depend on the number of turns of wire and on the pattern of winding.

$$R = \frac{\rho_w l_w}{A_w}. \tag{3.42}$$

3.2.5 Voltage and Power Generation

The magnetic fields in the system are linear; therefore superposition can be used and the total magnetic field is the sum of the magnetic fields from the magnets and the coils.

$$H_{total} = \begin{cases} -\nabla(\psi_{A(magnets)} + \psi_{(coils)}) & 0 \le x \le x_A. \\ -\nabla(\psi_{B(magnets)} + \psi_{(coils)}) & 0 \ge x \ge -x_B. \end{cases} \tag{3.43}$$

$$B_{total} = \mu_0 H_{total}.$$

The magnetic fluxes through the coils due to the magnets, $\lambda_{m(A)}$, $\lambda_{m(B)}$ and $\lambda_{m(C)}$ through phases A, B and C respectively, are calculated by multiplying the magnetic flux density and the area of the coils.

$$\begin{bmatrix} \lambda_{m(A)} \\ \lambda_{m(B)} \\ \lambda_{m(C)} \end{bmatrix} = \begin{bmatrix} B_{x(magnets)}A_A \\ B_{x(magnets)}A_B \\ B_{x(magnets)}A_C \end{bmatrix}$$

By superposition, the total magnetic flux through the coils is the sum of the fluxes generated by the magnets and by the flow of current through the coils.

$$\begin{bmatrix} \lambda_A \\ \lambda_B \\ \lambda_C \end{bmatrix} = \begin{bmatrix} \lambda_{c(A)} \\ \lambda_{c(B)} \\ \lambda_{c(C)} \end{bmatrix} + \begin{bmatrix} \lambda_{m(A)} \\ \lambda_{m(B)} \\ \lambda_{m(C)} \end{bmatrix} = \begin{bmatrix} L & -M & -M \\ -M & L & -M \\ -M & -M & L \end{bmatrix} \begin{bmatrix} i_A \\ i_B \\ i_C \end{bmatrix} + \begin{bmatrix} B_{x(magnets)}A_A \\ B_{x(magnets)}A_B \\ B_{x(magnets)}A_C \end{bmatrix} \tag{3.44}$$

In order for these equations to hold true, it is important that the magnetic backing of the coils does not saturate due to the magnetic flux through it. Figure 3-10 shows the path of the flux through the magnetically permeable backings. $B \cdot A$ should be calculated for the area under half a magnet, and should be equated to $B_{new} \cdot A_{new}$, where A_{new} is the cross-sectional area of the magnetic backing through which the flux will pass. A BH chart of the backing material should be consulted to confirm that B_{new} will not cause it to saturate. A similar

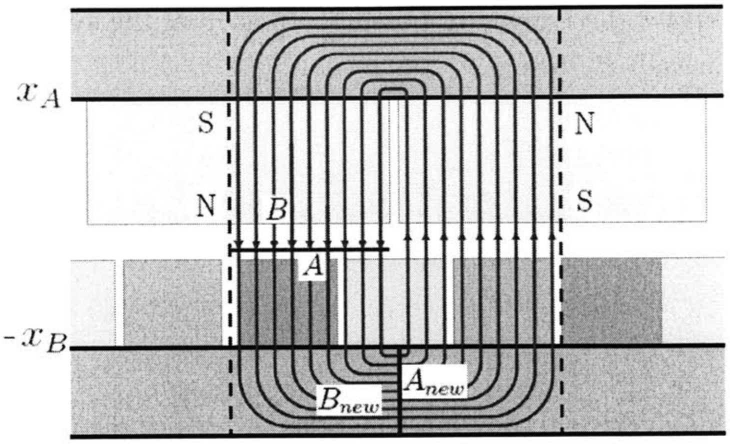

Figure 3-10: Path of the magnetic flux in a magnet-across-coils system.

check should be conducted for the backing of the magnets.

Faraday's law is invoked again in order to calculate the voltage generated across the coils. λ_A, λ_B and λ_C are known as a function of position, so $\frac{d\lambda}{dz}$ can be calculated for each phase. These values, when multiplied by the velocity of the coil ($\frac{dz}{dt}$), give $\frac{d\lambda}{dt}$ for each respective phrase. Since the phases are identical except for a displacement in space, the voltage through them will be identical except displaced in time.

$$\frac{d}{dt}\begin{bmatrix}\lambda_A\\ \lambda_B\\ \lambda_C\end{bmatrix} = \begin{bmatrix}V_A\\ V_B\\ V_C\end{bmatrix} - \begin{bmatrix}R & 0 & 0\\ 0 & R & 0\\ 0 & 0 & R\end{bmatrix}\begin{bmatrix}i_A\\ i_B\\ i_C\end{bmatrix} \tag{3.45}$$

Equations 3.44 and 3.45 give us a system of 9 equations and 9 variables: the variables are the magnetic fluxes, currents, and voltages for the three phases; the resistance, self-inductance, and mutual inductance of the coils are known.

Now that we can solve for the output voltage of the system, we consider the dissipation of the power produced. Applying Ohm's law to the system connected to a load resistor R_L gives:

$$\begin{bmatrix}V_A\\ V_B\\ V_C\end{bmatrix} = -\begin{bmatrix}R_L & 0 & 0\\ 0 & R_L & 0\\ 0 & 0 & R_L\end{bmatrix}\begin{bmatrix}i_A\\ i_B\\ i_C\end{bmatrix} \tag{3.46}$$

If $R \gg \omega L$, where ω is the operating frequency of the system in rad/s, the effect of inductances L and M is negligible compared to that of the resistance R. An argument similar to the one presented in Section 3.1.3 leads to the conclusion that R_L should be equal to R in order to extract the maximum possible power from the system, the instantaneous power dissipated through R_L being:

$$\begin{bmatrix} P_A \\ P_B \\ P_C \end{bmatrix} = \frac{R_L}{(R+R_L)^2} \begin{bmatrix} V_A^2 \\ V_B^2 \\ V_C^2 \end{bmatrix} \tag{3.47}$$

3.3 Summary

The focus of this chapter was to develop equations to predict the open-circuit voltage and power output of magnetic induction systems as a function of their geometry and material properties. Two types of systems, magnet-through-coil and magnet-across-coils, were analyzed.

The open-circuit voltage and power output generated by a magnet-through-coil system, from Equations 3.13 and 3.16 respectively, are:

$$V = -\int \frac{vN(\phi_1+\phi_2)}{l_c}\Big|_h^{h+l_c} dA.$$

$$P = \frac{R_L V^2}{(R_c+R_L)^2}$$

The open-circuit voltage and power output of a three phase magnet-across-coils system, from Equations 3.45 and 3.47 respectively, are:

$$\begin{bmatrix} V_A \\ V_B \\ V_C \end{bmatrix} = -\begin{bmatrix} R_L & 0 & 0 \\ 0 & R_L & 0 \\ 0 & 0 & R_L \end{bmatrix} \begin{bmatrix} i_A \\ i_B \\ i_C \end{bmatrix}$$

$$\begin{bmatrix} P_A \\ P_B \\ P_C \end{bmatrix} = \frac{R_L}{(R+R_L)^2} \begin{bmatrix} V_A^2 \\ V_B^2 \\ V_C^2 \end{bmatrix}$$

These equations are for the instantaneous power dissipation through a load resistor. When the input displacement is sinusoidal, the output voltage will also be a sinusoid of the same frequency; then the average power dissipated over a cycle is half of the maximum instantaneous power generated.

A magnet-across-coils system can generate higher voltage than a magnet-through coils system for the same stroke, because the former system can cause complete flux reversals across the coils. Although harder to manufacture, a magnet-across coils system is more suited for applications where space is limited, and hence it was selected for the prototype of the system to harvest energy form car door vibrations. The next chapter discusses the development of the other components of the energy harvesting system.

Chapter 4

Energy Harvesting System Design

This chapter gives an overview of the theory behind all steps of the design process for a magnet-across-coils style magnetic induction system that harvests energy from mechanical vibrations. The chapter is divided into four sections. The first section presents the derivation of an equation for the maximum power that can be extracted from a surface vibrating at a given frequency and amplitude. This equation can be used to determine the feasibility of using car door vibrations as an energy source for power window and lock operation. The second section connects the magnetic induction system to the overall mass-spring-damper system, and the third section describes the equations for the design of the cantilever beam prototype that was built and tested. The last section discusses the equations for energy storage in a capacitor.

4.1 Vibration Analysis

This section derives a formula for the power that can be harvested through the damper in a mass-spring-damper system attached to a vibrating surface. The power dissipated through the damping element when the parameters of the system are optimized is the upper bound on the power that can be harvested from the system by extracting power through a damping element. Figure 4-1 shows a schematic of the system being analyzed and Table 4.1 lists the variables in the system.

The parameters of the system are the mass m with position coordinate x. The mass is suspended by a spring with spring constant k and a damper with damping coefficient b from a vibrating surface with position coordinate y. From the force balance for the mass,

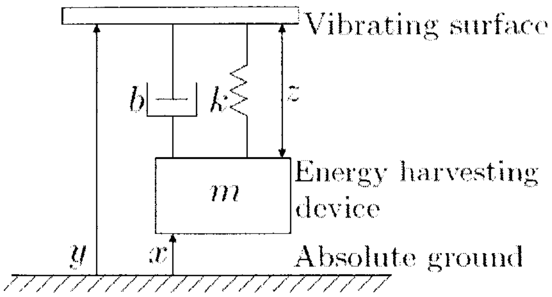

Figure 4-1: Schematic of a vibrating mass with a spring and damper.

Symbol	Units	Variable
b	Ns/m	Damping coefficient of the damper
k	N/m	Spring constant of the spring
m	kg	Vibrating mass
x	m	Position coordinate for the vibrating mass
y	m	Position coordinate for the vibrating surface
z	m	Position coordinate for relative motion between surface and mass
P	W	Average power dissipated through the damper
ω	rad/s	Frequency of vibration

Table 4.1: Nomenclature for Vibration Analysis

we obtain Equation 4.1, which can be simplified to Equation 4.2.

$$m\ddot{x} + b\dot{x} + kx = b\dot{y} + ky. \tag{4.1}$$

$$m\ddot{x} + b(\dot{x} - \dot{y}) + k(x - y) = 0. \tag{4.2}$$

Defining a new parameter z, which is the relative distance between the vibrating surface and the mass, we obtain Equations 4.3 and 4.4.

$$z = x - y. \tag{4.3}$$

$$m\ddot{z} + b\dot{z} + kz = -m\ddot{y}. \tag{4.4}$$

In order to maximize the power output through the damper, we choose a spring constant such that the mass and spring are in resonance. This gives us Equation 4.5, which when combined with Equation 4.4 leads to Equation 4.6.

$$m\ddot{z} + kz = 0. \tag{4.5}$$

$$b\dot{z} = -m\ddot{y}. \tag{4.6}$$

Taking the Laplace transform of these equations and substituting $s = j\omega$ to represent a sinusoidal input of frequency ω yields

$$ms^2z + kz = 0 \;\Rightarrow\; m(j\omega)^2z + kz = 0. \tag{4.7}$$

$$bsz = -ms^2y \;\Rightarrow\; bj\omega z = -m(j\omega)^2y. \tag{4.8}$$

Equating the magnitudes of both sides of Equation 4.8, we obtain Equation 4.9.

$$b\omega z = m\omega^2y. \Rightarrow b = \frac{m\omega y}{z}. \tag{4.9}$$

The instantaneous power dissipated through a damper is the product of the damping force on the mass, $b\omega z$, and the velocity of the mass, ωz. The time-average of the power, P, extracted for a sinusoidal input is half of the maximum instantaneous power. Substituting Equation 4.9 in Equation 4.10 gives us Equation 4.11, which is a formula for the maximum time-averaged power that can be extracted through a damper for a given mass, vibration frequency, input amplitude, and output amplitude relative to the vibrating surface.

$$P = \frac{1}{2}(b\omega z)(\omega z) = \frac{b\omega^2z^2}{2}. \tag{4.10}$$

$$P = \frac{m\omega^3yz}{2}. \tag{4.11}$$

The upper bound on the power that can be harvested from a vibrating surface is a function of the vibration frequency, input and output amplitude, and vibration mass. Equation 4.11 helps us understand how the system parameters impact the output power, and can be used as a guide for the design and optimization of an energy harvesting system.

4.2 Magnetic Induction System as a Damping Element

The damping element in a vibration system can be effectively realized as a magnetic induction system. This allows the energy dissipated in the damper to be harvested as electrical energy. However, it is impossible to eliminate damping from other sources in a physical system. Hence the damping term from Figure 4-1 is separated into two terms: internal (b_I) and external (b_E). The external damping term is the contribution from the magnetic induction system and represents the conversion and harvesting of useful power. The internal damping includes the damping from other factors which are all losses. Equation 4.6 can now be extended as

$$(b_I + b_E)\dot{z} = -m\ddot{y}.$$

For a given input vibration, since m and $\ddot{y}$ are fixed, this means that

$$\dot{z} \propto \frac{1}{b_I + b_E}. \tag{4.12}$$

The average power dissipated through damper is half of the product of the damping force and the velocity of the mass, so the average power dissipated through the external damper, representing the useful harvested power, is

$$P_{b_E} = \frac{b_E \dot{z}^2}{2} \propto \frac{b_E}{(b_E + b_I)^2}. \tag{4.13}$$

For a given b_I, P_{b_E} is a function of b_E. In order to find the maxima of P_{b_E}, we differentiate it with respect to b_E and obtain:

$$\frac{dP_{b_E}}{db_E} = \frac{d}{db_E}\frac{b_E}{(b_I + b_E)^2} = 0.$$

$$\Rightarrow \quad \frac{1}{(b_I + b_E)^2} - \frac{2b_E}{(b_I + b_E)^3} = 0. \Rightarrow (b_I + b_E) - 2b_E = 0.$$

$$\Rightarrow b_E = b_I. \tag{4.14}$$

Hence, once b_I of a system is fixed, b_E should be matched to it in order to maximize the power dissipated through the external damping element.

Since b_I is a function of the physical system used to implement the spring and damper, it is partially controllable through the design of the physical system. Equation 4.13 implies that it is desirable to build a system with a low b_I to increase P_{b_E}; however, since $\dot{z}$ is inversely proportional to $(b_I + b_E)$ from Equation 4.12, making the damping arbitrarily small will cause a large increase in $\dot{z}$. A large increase in $\dot{z}$ would lead to a proportional increase in z, because $|\dot{z}| = z\omega$ and ω is a constant. An arbitrarily large z will cause the physical system will fail because of plastic deformation. Therefore, the reduction of b_I is not necessarily the limiting factor on the performance of a vibrating system; the maximum allowable displacement should also be considered.

Symbol	Units	Variable
c	m	Maximum distance of the beam profile from the neutral axis
k	N/m	Spring constant of the cantilever beam
z	m	Maximum deflection of the cantilever beam
D	m	Diameter of the cantilever beam
E	N/m^2	Young's Modulus of the beam material
I_x	m^4	Moment of Inertia of the beam profile about the x-axis
I_y	m^4	Moment of Inertia of the beam profile about the y-axis
L	m	Length of the cantilever beam
M	Nm	Moment on the cantilevered beam
R	m	Radius of the cantilever beam
σ_{max}	N/m^2	Maximum stress in the cantilever beam when deflected
σ_y	MPa	Yield stress of the cantilever beam
θ_C	rad	Angle defining the beam profile (marked in Figure 4-2)

Table 4.2: Nomenclature for Cantilever Beam design

4.3 Cantilever Beam as a Spring Element

This section describes the implementation of the mass and spring components of the system. The cantilever beam with a mass on the end is a simple design with a low part-count for easy manufacture. The length, profile and material of the beam determine the spring constant, and the magnetic induction system is mounted on the mass attached at the end of the beam as the damping component. Table 4.2 lists the variables of the system.

4.3.1 Beam Profile

The cross-sectional profile of the beam is important because it affects the moment of inertia and hence the spring constant of the beam. A round profile has the advantage of being easy to press-fit into a hole, which results in excellent attachment stiffness at a low cost; the disadvantage is that there is no directional selectivity.

A round beam with material shaved off to form the profile shown in Figure 4-2 provides different moments of inertia in different directions and can still be press-fit into a hole. The origin is the center of the round beam of radius R. θ_C is the angle between the x-axis and the line from the origin to the highest point of the flat surface created by shaving material off the round beam. The directional selectivity provided by this profile ensures that the magnets will move across the coils in the direction intended, thus maximizing the power output from a given vibration.

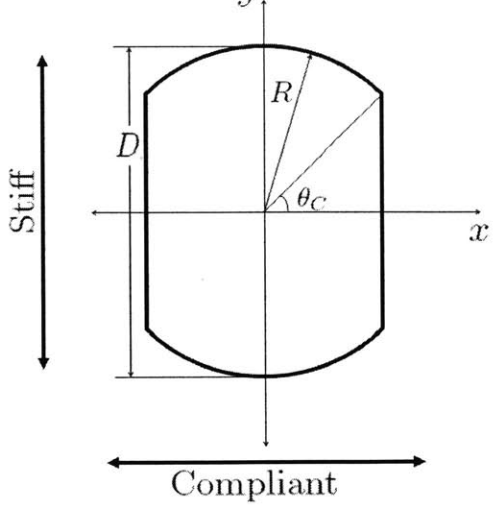

Figure 4-2: Profile of the cantilever beam.

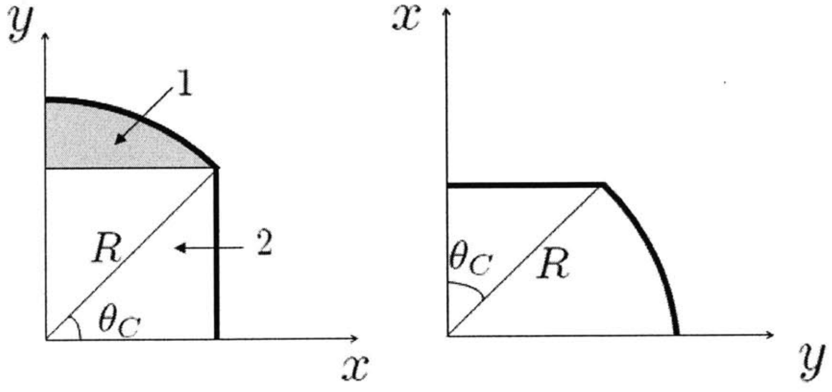

(a) Profile for calculation of I_x.

(b) Profile for calculation of I_y.

Figure 4-3: Profiles for calculation of I_x and I_y.

The moment of inertia about the x-axis is defined as:

$$I_x = \int y^2 dA. \tag{4.15}$$

Due to symmetry, the moment of inertia for the beam is four times the moment of inertia of a quarter of the beam as shown in Figure 4-3(a). The moment of inertia for the quarter beam is calculated by separating the profile into two regions and adding their moments of inertia.

$$\begin{cases} x = R\cos\theta_C & 0 \leq \theta \leq \theta_C. \\ x = R\cos\theta,\ y = R\sin\theta & \theta_C \leq \theta \leq \pi/2. \end{cases}$$

$$I_x = 4[\int_0^{R\sin\theta_C} y^2 R\cos\theta_C dy + \int_{\theta_C}^{\pi/2} R^4(\sin\theta)^2(\cos\theta)^2 d\theta]$$

$$I_x = 4[R\cos(\theta_C)[\frac{y^3}{3}]_0^{R\sin\theta_C} + \frac{R^4}{32}[4\theta_C - \sin 4\theta_C]_{\theta_C}^{\pi/2}]$$

$$I_x = \frac{4R^4\cos\theta_C(\sin\theta_C)^3}{3} + \frac{R^4(2\pi - 4\theta_C + \sin 4\theta_C)}{8} \tag{4.16}$$

Similarly, the moment of inertia about the y-axis is defined as:

$$I_y = \int x^2 dA. \tag{4.17}$$

Due to symmetry, the moment of inertia for the beam is four times the moment of inertia of a quarter of the beam as shown in Figure 4-3(b).

$$x = R\cos\theta,\ y = R\sin\theta\ for\ 0 \leq \theta \leq \pi/2 - \theta_C.$$

$$I_y = 4[\int_0^{\pi/2-\theta_C} R^4(\sin\theta)^2(\cos\theta)^2 d\theta]$$

$$I_y = 4[\frac{R^4}{32}[4\theta_C - \sin 4\theta_C]_0^{\pi/2-\theta_C}]$$

$$I_y = \frac{R^4(2\pi - 4\theta_C + \sin 4\theta_C)}{8} \tag{4.18}$$

The ratio of the two moments of inertia is :

$$\frac{I_x}{I_y} = 1 + \frac{32\cos\theta_C(\sin\theta_C)^3}{3(2\pi - 4\theta_C + \sin 4\theta_C)}. \tag{4.19}$$

Figure 4-4 is the plot of I_x and I_y for R=1 and θ_C varying from 0° to 70°. Figure 4-5 shows the magnitude of the I_x/I_y ratio for R=1 and θ_C varying from 0° to 70°. As can be seen from the plots, an angle of $\theta_C = 45°$ results in an I_x/I_y ratio of almost 2. At the same time, enough material is left on the circumference to ensure a good press-fit. For these reasons, $\theta_C = 45°$ was selected to define the beam profile shape.

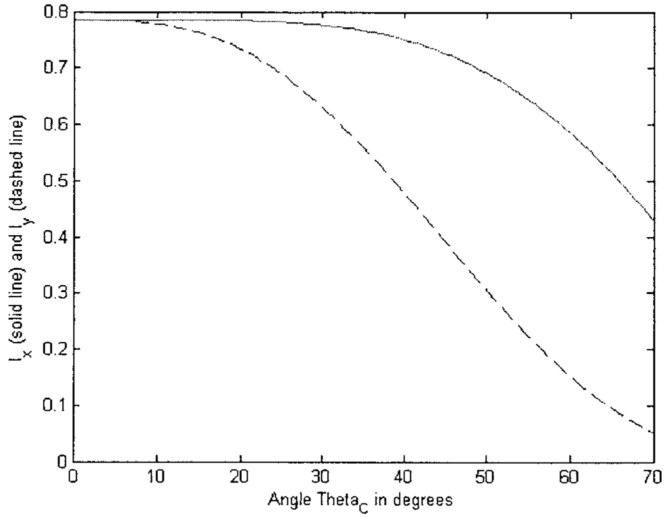

Figure 4-4: I_x (solid line) and I_y (dashed line) for R=1 and θ_C varying from 0° to 70°.

4.3.2 Cantilever Beam Design

The cantilever beam must now be designed to function as the spring element in the energy harvesting system. The input vibration frequency and amplitude are known. We know the power output required, and the allowable amplitude, so from Equation 4.11 we can calculate the mass we need to vibrate to extract the required power.

Now we consider a simple cantilevered beam with a mass at the end. The stiffness equation for a simply supported beam is

$$k = \frac{3EI_y}{L^3}, \tag{4.20}$$

where k is the beam stiffness, E is the Young's modulus of the beam material, I_y is the moment of inertia, and L is the length of the beam. From Equation 4.5, we know that k

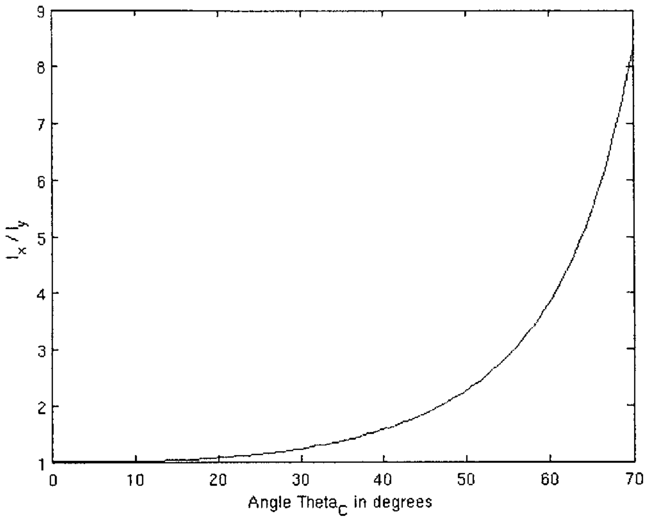

Figure 4-5: Ratio of I_x to I_y for R=1 and θ_C varying from 0° to 70°.

must equal $m\omega^2$. The moment of inertia for a profiled beam with parameters D and θ_C is

$$I_y = \frac{D^4(2\pi - 4\theta_C + \sin 4\theta_C)}{128}, \tag{4.21}$$

It is important for the beam to withstand many cycles without failing due to fatigue, and hence stresses greater than half of the yield stress (σ_y) should not be imposed on the beam. Thus, the length of the beam is also governed by the maximum stress allowable in the beam material σ_{max}:

$$\sigma_{max} = \frac{Mc}{I_y}, \tag{4.22}$$

where M is the bending moment applied to the beam, and c is the maximum distance from the neutral axis. For the profiled beam,

$$c = \frac{D \cos \theta_C}{2}, \tag{4.23}$$

$$M = kzL. \tag{4.24}$$

Combining Equations 4.20 through 4.24, we get

$$D = [\frac{6144 E m^2 z^3 (\cos \theta_C)^3 \omega^4}{\sigma_{max}^3 (2\pi - 4\theta_C + \sin 4\theta_C)^2}]^{\frac{1}{5}}, \tag{4.25}$$

Variable	Numerical Value	Units	Description
m	1.2	kg	Mass on the end of the cantilever beam
D	12.7	mm	Diameter of the cantilever beam
E	207	GPa	Young's Modulus of the beam material
L	210	mm	Length of the cantilever beam
θ_C	45	$^\circ$	Angle defining the beam profile (Figure 4-2)
σ_y	0.7	GPa	Yield stress of the cantilever beam

Table 4.3: Parameter values of the parts used for the cantilever beam component of the energy harvesting prototype.

$$L = \frac{\sigma_{max} D^3 (2\pi - 4\theta_C + \sin 4\theta_C)}{64 m z \cos\theta_C \omega^2}. \tag{4.26}$$

For $\theta_C = 45^\circ$, the equations simplify to

$$D_{45^\circ} = [\frac{1536\sqrt{2} E m^2 z^3 \omega^4}{\sigma_{max}^3 \pi^2}]^{\frac{1}{5}}, \tag{4.27}$$

$$L_{45^\circ} = \frac{\sqrt{2}\pi \sigma_{max} D_{beam}^3}{64 m \omega^2 z}. \tag{4.28}$$

The equations above were used for the design of a prototype energy harvesting system. The dimensions of the cantilever beam system are given in Table 4.3 and Figure 4-6 shows a solid model assembly of the cantilever system parts. Drawings of the parts can be found in Appendix B.

4.4 Energy Storage

The voltage generated by a magnetic induction system can be used to charge an energy-storage device such as a capacitor. The characteristics of the system affect the capacitor charging circuit. For a single phase output, the circuit model depends on whether the coil resistance or coil inductance is dominant.

If the inductance of the coil is negligible compared to its resistance ($R \gg \omega L$), the magnetic flux induced due to the flow of current through the coil can be considered insignificant compared to the magnetic flux from the magnet. The charging of the capacitor can then be modeled by a simple RC circuit with an ideal diode preventing the discharge of the capacitor. The rectified voltage waveform is the input to the capacitor charging circuit. Figure 4-7 shows a schematic of the capacitor charging circuit.

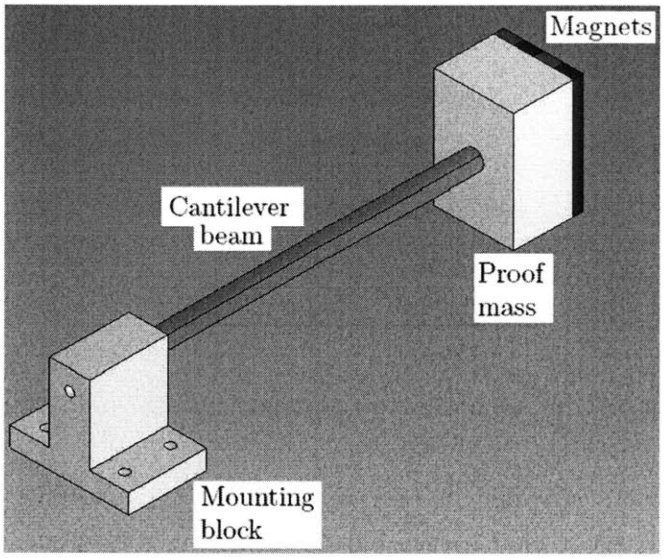

Figure 4-6: An isometric view of the cantilever beam subsystem of the energy harvesting prototype. The magnets are attached to a mass on the end of the cantilever beam.

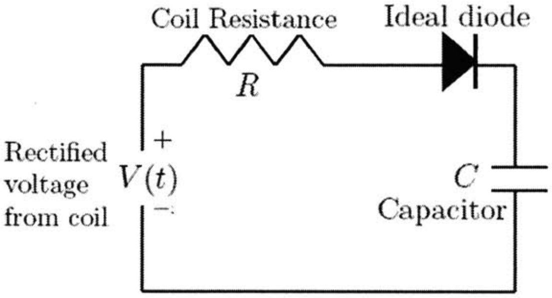

Figure 4-7: Capacitor charging circuit schematic.

Every voltage cycle will add charge to the capacitor reservoir. The charge added to the capacitor during the n^{th} cycle, q_n, can be calculated by integrating the current flowing through the capacitor branch of the circuit, as shown by the shaded area in Figure 4-8. If the magnitude of C is very large (as required to store large amounts of energy), the change in voltage across the capacitor during a charging cycle can be assumed to be negligible, and the voltage of the capacitor during the n^{th} cycle can be represented by a constant, V_n. Then,

$$CV_{n+1} = CV_n + q_n, \tag{4.29}$$

$$q_n = \int \frac{V(t) - V_n}{R}. \tag{4.30}$$

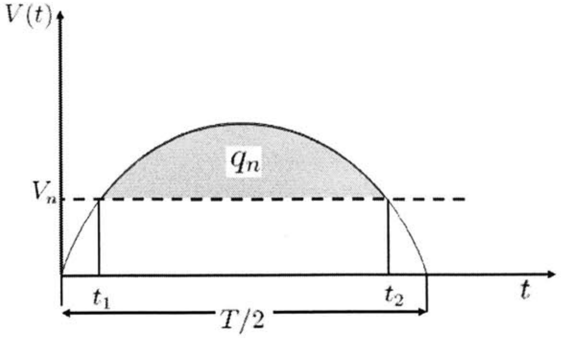

Figure 4-8: Charge added to the capacitor over a charging cycle.

The amount of charge added to the capacitor during a charging cycle depends on the voltage to which the capacitor has already been charged. Thus, each charging cycle adds less and less charge to the capacitor.

Combining Equations 4.29 and 4.30 gives a difference equation that can be solved iteratively to calculate the number of charging cycles required to store a given amount of energy in the capacitor, giving us

$$CV_{n+1} = CV_n + \int \frac{V(t) - V_n}{R} dt.$$

Assuming a sinusoidal form for the input voltage,

$$V(t) = V_0 \sin(\omega t),$$

$$CV_{n+1} = CV_n + \int \frac{V_0 \sin(\omega t) - V_n}{R} dt.$$

Charge is accumulated only when the value of $V(t)$ is greater than V_n (from t_1 to t_2 as marked in Figure 4-8). Including the appropriate limits of integration gives:

$$CV_{n+1} = CV_n + \int_{t_1}^{t_2} \frac{V_0 \sin(\omega t) - V_n}{R} dt.$$

Now we express t_1 and t_2 in terms of V_0, V_n, and ω:

$$At\ t_1 : \ V(t_1) = V_0 \sin(\omega t_1) = V_n \Rightarrow t_1 = \frac{1}{\omega} \sin^{-1}(\frac{V_n}{V_0})$$

By symmetry, $t_2 = T/2 - t_1$. Combining this with $T = 2\pi/\omega$, we get:

$$t_2 = \frac{T}{2} - \frac{1}{\omega}\sin^{-1}(\frac{V_n}{V_0}) \Rightarrow t_2 = \frac{1}{\omega}\sin^{-1}(\frac{V_n}{V_0})$$

$$\Rightarrow CV_{n+1} = CV_n + \int_{\frac{1}{\omega}\sin^{-1}(\frac{V_n}{V_0})}^{\frac{1}{\omega}[\pi-\sin^{-1}(\frac{V_n}{V_0})]} \frac{V_0\sin(\omega t) - V_n}{R}dt.$$

Normalizing over a time period leads to substitution of variables:

$$\tilde{t} \equiv \frac{t}{T} = \frac{\omega t}{2\pi}$$

$$CV_{n+1} = CV_n + \frac{2\pi}{\omega}\int_{\frac{1}{2\pi}\sin^{-1}(\frac{V_n}{V_0})}^{\frac{1}{2\pi}[\pi-\sin^{-1}(\frac{V_n}{V_0})]} \frac{V_0\sin(2\pi\tilde{t}) - V_n}{R}d\tilde{t}.$$

Define a new variable $X_n \equiv V_n/V_0$.

$$\frac{RC}{T}X_{n+1} = \frac{RC}{T}X_n + \int_{\frac{1}{2\pi}\sin^{-1}(X_n)}^{\frac{1}{2\pi}(\pi-\sin^{-1}(X_n))} (\sin(2\pi\tilde{t}) - X_n)d\tilde{t}.$$

$$X_{n+1} = X_n + \frac{1}{2\pi(\frac{RC}{T})}\Big[\cos(\sin^{-1}(X_n)) - \cos(\pi - \sin^{-1}(X_n)) - X_n(\pi - 2\sin^{-1}(X_n))\Big]. \quad (4.31)$$

Equation 4.31 represents a family of curves dependent on the value of $\frac{RC}{T}$. Figure 4-9 shows the charging curves for some values of $\frac{RC}{T}$.

The rate of energy harvesting can be calculated by dividing the energy stored after n cycles by the time taken to complete n storage cycles.

4.5 Summary

The components of a mass-spring-damper energy harvesting system were discussed in this chapter. The theory behind each component was presented and a prototype was designed for testing. The next chapter discusses the MATLAB models that were used to predict the voltage and power output of the prototype.

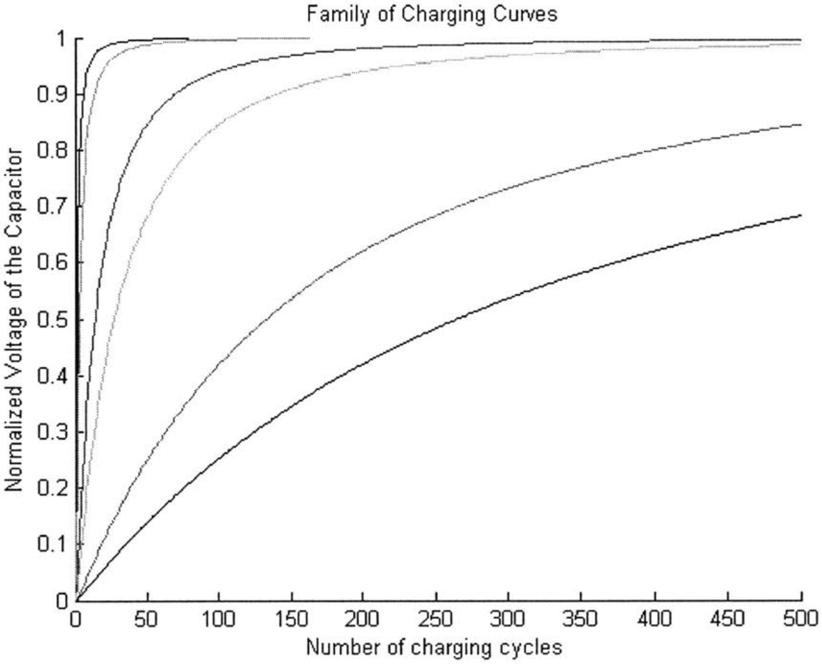

Figure 4-9: Normalized charging curves for various values of $\frac{RC}{T}$. The values of $\frac{RC}{T}$, from the fastest to slowest growing curve, are 0.5, 1, 5, 10, 50 and 100.

Chapter 5

Simulation

MATLAB models were created to simulate the magnetic fields generated by the magnets and coils in various configurations and to calculate the voltage generated by relative movement of the magnets and coils. This chapter describes the MATLAB models created for magnet-through-coil and magnet-across-coils systems and their predictions. The MATLAB code is included in Appendix A.

5.1 Magnet-through-coil Simulation

This section describes the predictions made by the model created to predict the magnetic fields and voltages produced by the motion of a magnet through a coil.

5.1.1 Single Turn of Wire

Figure 5-1 graphs the magnitude of the magnetic flux (as a function of y) which a monopole of magnitude 1 Wb causes to flow through one turn of wire of diameter 1 cm placed at y. Note the discontinuity at the monopole location due to the sudden change in the direction of the flux through the coil. Equations 3.5 and3.6 were used to generate this plot.

The total magnetic flux through the turn of wire due to a bar magnet is obtained by adding the contributions of the two monopoles and the magnetization of the magnet. The magnetic flux through a wire turn of diameter 1 cm due to a bar magnet with monopoles of magnitude 1 Wb each placed at ±1 cm from the origin is shown in Figure 5-2, which graphs Equation 3.8.

The derivative of the magnetic flux with respect to position is shown in Figure 5-3.

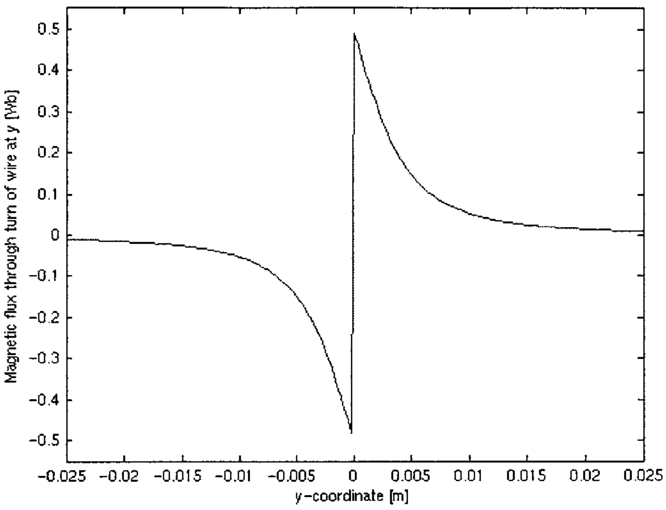

Figure 5-1: Magnetic flux through 1 cm diameter turn of wire due to a magnetic monopole of magnitude 1 Wb placed at the origin.

Variable	Numerical Value	Units	Description
a	3	cm	Vibration amplitude
d_c	1	cm	Average diameter of the coil
f	1	Hz	Vibration frequency
l_c	2	cm	Height of the coil
l_m	2	cm	Height of the magnet
N	2500	–	Number of turns of wire in a coil
$\mu_0 M$	1.2	T	Magnetization flux density of the magnet

Table 5.1: Numerical values for input variables used in the simulation of the magnet-through-coils induction system. The descriptions of all the system variables are in Table 3.1.

The expected voltage across a turn of wire, from Equation 3.11, for a sinusoidal input velocity is shown in Figure 5-4.

5.1.2 Coil of Wire

This subsection describes the predictions made by the model for the voltage across a coil consisting of many turns of wire. Table 5.1 lists the numerical values used for the input variables.

Figure 5-5 graphs the magnitude of the change in magnetic flux (as a function of y) which a bar magnet of length 2 cm and magnetization flux density 1.2 T causes to flow through

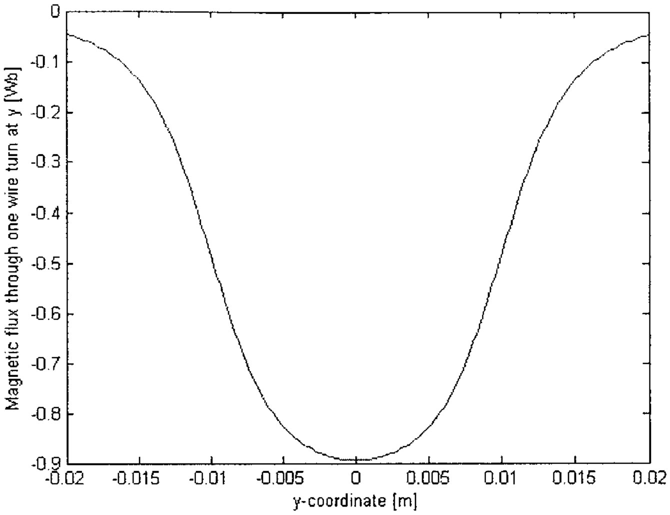

Figure 5-2: Magnetic flux through 1 cm diameter turn of wire due to a bar magnet with poles of magnitude 1 Wb placed at ±1 cm.

a coil with 2500 turns of wire, length 2 cm, and average diameter 1 cm, when the lowest edge of the coil is placed at y. The predicted voltage generation, from Equation 3.13, for a sinusoidal velocity input is shown in Figure 5-6.

5.2 Magnet-across-coils Simulation

This section describes the model created to predict the magnetic fields and voltages produced by the motion of magnets across coils. Table 5.2 lists the numerical values used for the input variables of the system to produce the plots in this section. These values correspond to the parameters of the prototype system.

A major assumption built into the MATLAB model is that the inductive effects are negligible compared to the effects of the resistance ($R \gg \omega L$). This assumption is checked in the code once the values for L and R are calculated, and the code will issue a warning that the results are not accurate if the condition is not satisfied.

5.2.1 Magnetic Field Generated by the Magnets

The magnetic fields due to the magnets depend on the charge density generated by the magnets at the $x = 0$ plane. Figure 5-7 shows the sum of the first 100 terms of the Fourier

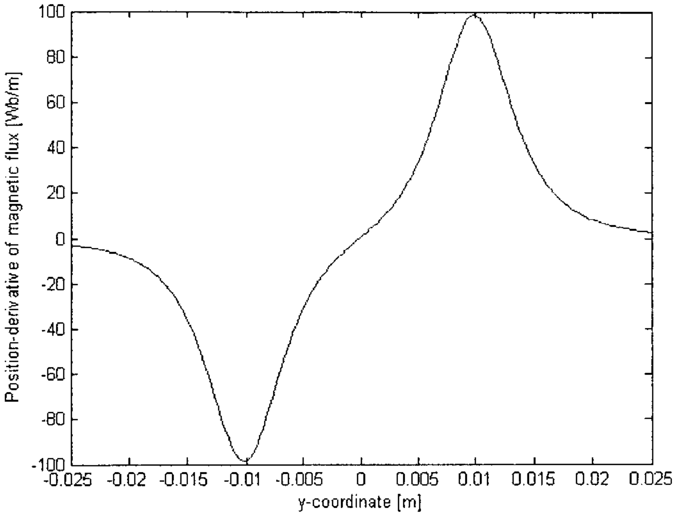

Figure 5-3: The derivative with respect to position of the magnetic flux (proportional to the voltage generated across the coil) through a 1 cm diameter turn of wire due to a bar magnet with poles of magnitude 1 Wb placed at ±1 cm.

series from Equation 3.18. This sum was used to approximate the charge density waveform at plane $x = 0$.

The magnetic potential generated by the magnets in Regions A and B, from Equations 3.31 and 3.32, are plotted in Figures 5-8 and 5-9 respectively. Figure 5-10 is a contour plot of the magnetic potential in both regions.

5.2.2 Magnetic Field Generated by Coil Current

The magnetic fields generated by the flow of current through the coils must be calculated in order to calculate the self and mutual inductances of the coils. Figure 5-11 plots the magnetic potential created by the flow of a $1A$ current through the phase A coils of the magnet-across-coils induction system, as predicted by Equation 3.38. Note that the potential created is three orders of magnitudes lower than that created by the magnets. Figure 5-12 shows a contour plot of the magnetic potential generated by the $1A$ current through the phase A coils.

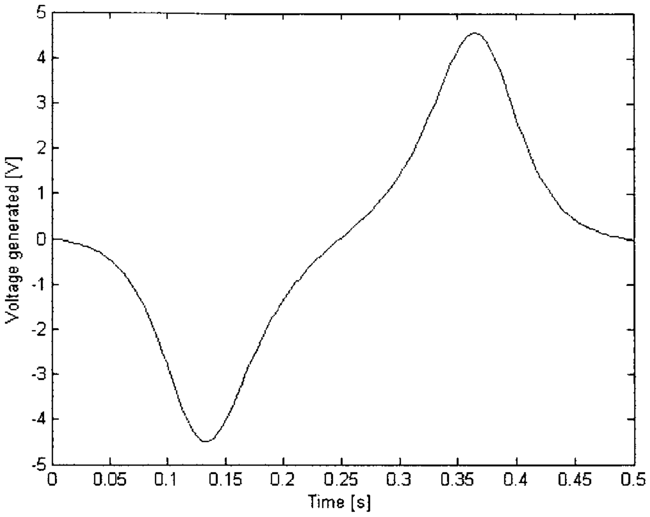

Figure 5-4: Prediction of voltage generated when a bar magnet with poles of magnitude 1 Wb placed at ±1 cm moves through a turn of wire of diameter at a frequency of 1 Hz and amplitude of ± 1 cm.

5.2.3 Voltage generation

The vibration input is a 30 Hz sinusoid with 3 mm amplitude. Figure 5-13 shows the position and velocity of the magnets over half a vibration cycle.

The magnetic flux through phase A coils and the voltage generated across them, as predicted by Equations 3.44 and 3.45, are plotted in Figures 5-14 and 5-15 respectively.

One of the advantages of the MATLAB model was that it enabled a sensitivity analysis of the power and voltage to the variables in the system. Because the equations are complicated, it is hard to develop intuition about the dependence of the output voltage and power on different system parameters. The MATLAB model used Equations 3.45 and 3.47 to create the plots in Figures 5-16 and 5-17, which are useful for sensitivity analysis and optimization.

5.3 Summary

This chapter presented some of the results from the MATLAB Simulations. The MATLAB code can be found in Appendix A. The models were used to predict the open-circuit voltage of specific magnet-through-coil and magnet-across-coils systems. The next chapter describes the experiments that were conducted to test these predictions.

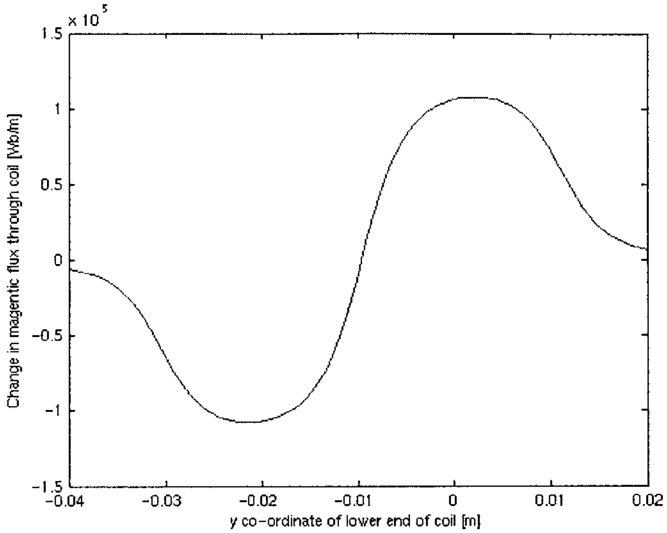

Figure 5-5: The derivative of the magnetic flux through a coil with 2500 turns of wire, length 2 cm and average diameter 1 cm, due to a bar magnet with magnetization flux density of 1.2 T and length 2 cm.

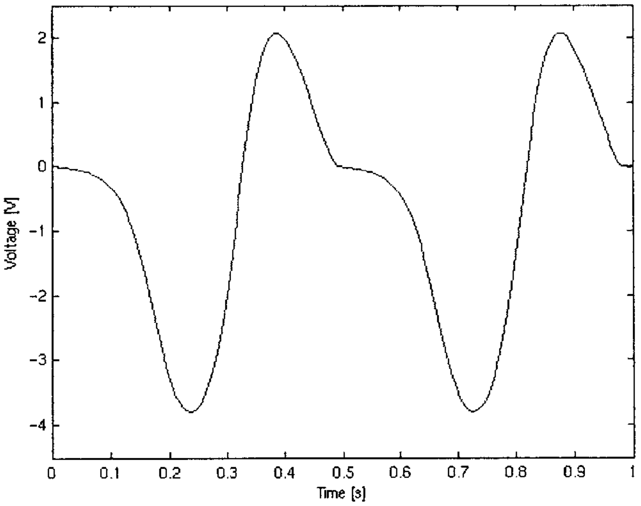

Figure 5-6: Prediction of voltage generated when a bar magnet with magnetization flux density 1.2 T and length 2 cm moves through a turn of wire of diameter at a frequency of 1 Hz and amplitude of 3 cm.

Variable	Numerical Value	Units	Description
a	3	mm	Vibration amplitude
d	0	mm	Gap between adjacent magnets
f	30	Hz	Vibration frequency
l	12.7	mm	Length of a magnet in the z direction
n	4	–	Number of magnetic poles in the system
r_w	0.4	mm	Radius of the wire used for coils
t	0.68	mm	Gap between adjacent coils
w	76.2	mm	Width of a magnet
x_A	6.35	mm	x-coordinate of magnet-steel interface
x_B	4	mm	x-coordinate of coil-steel interface
N	8	–	Number of turns of wire in a coil
N_F	100	–	Number of Fourier series terms summed
μ_0	$4\pi \times 10^{-7}$	Tm/A	Magnetic permeability of air
ρ	1.68^{-8}	Ωm	Resistivity of wire material
σ_{max}	1.31	T	Magnetic charge density of the magnets

Table 5.2: Numerical values for input variables used in the simulation of the magnet-across-coils induction system. The descriptions of all the system variables are in Table 3.2.

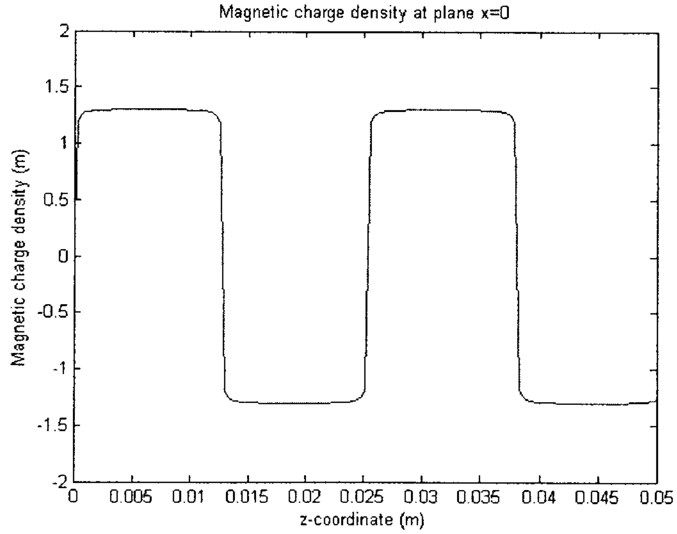

Figure 5-7: Magnetic charge density in plane $x = 0$ due to magnets.

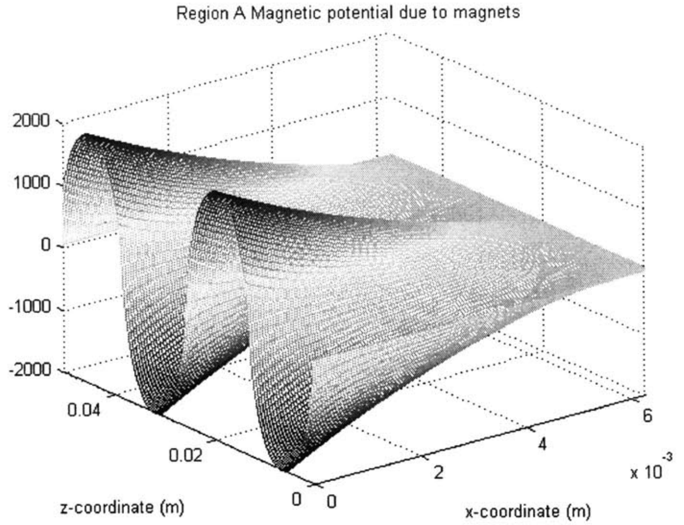

Figure 5-8: Magnetic potential in Region A due to magnets.

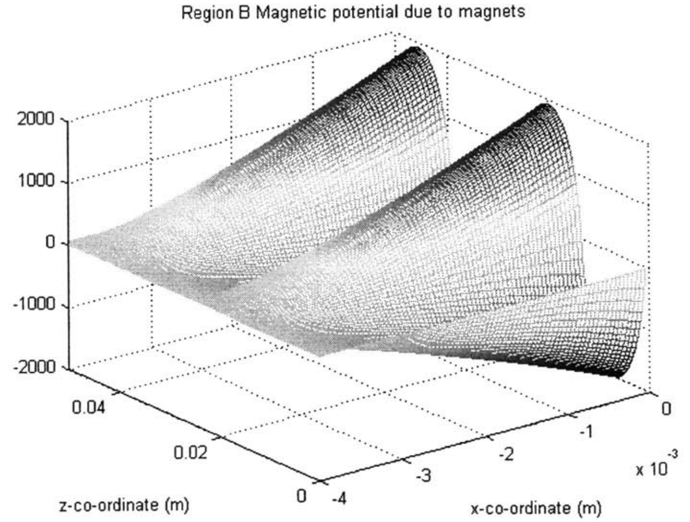

Figure 5-9: Magnetic potential in Region B due to magnets.

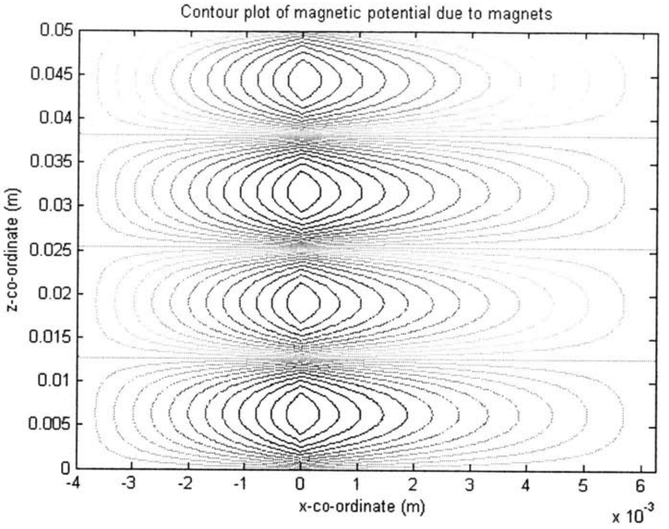

Figure 5-10: Contour plot of magnetic potential due to magnets.

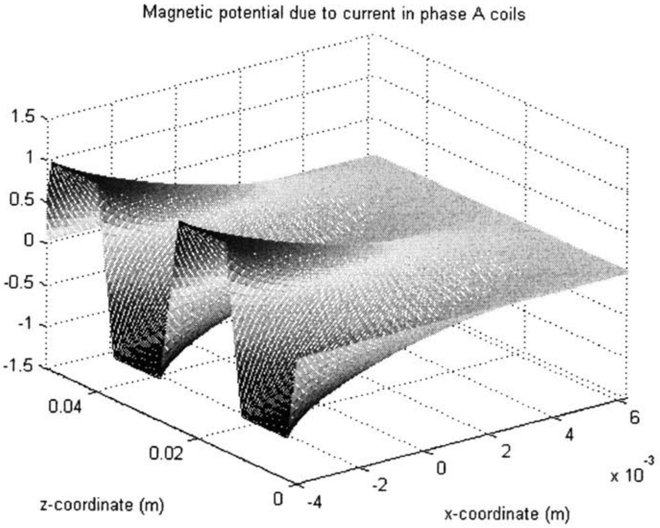

Figure 5-11: Magnetic potential due to a 1A current through the phase A coil.

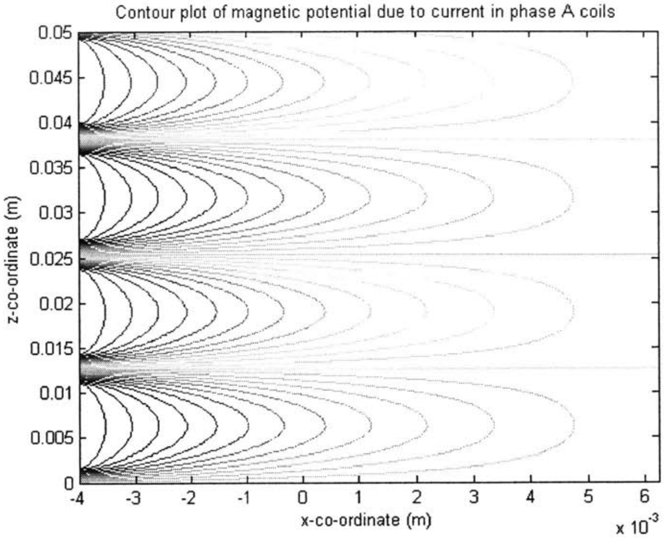

Figure 5-12: Contour plot of the magnetic potential due to a 1A current through the phase A coil.

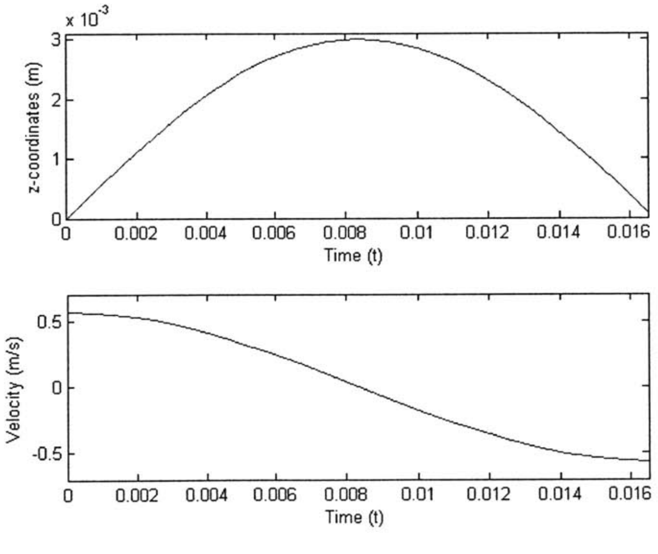

Figure 5-13: Position and velocity of the magnets over a half a vibration cycle.

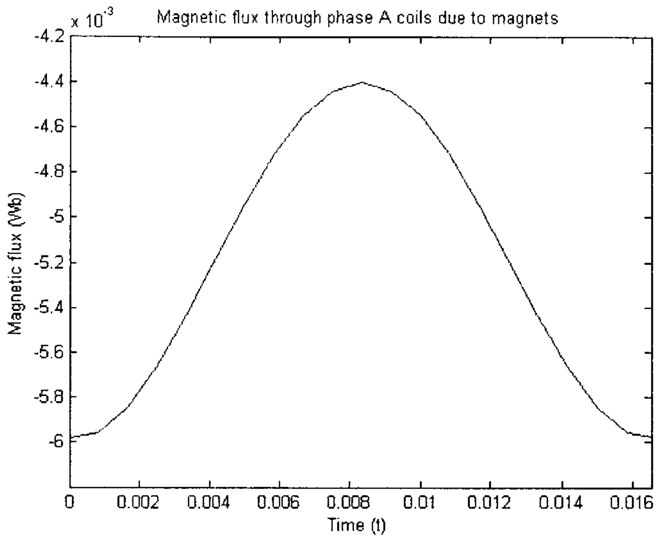

Figure 5-14: Magnetic flux through phase A coils over a half a vibration cycle.

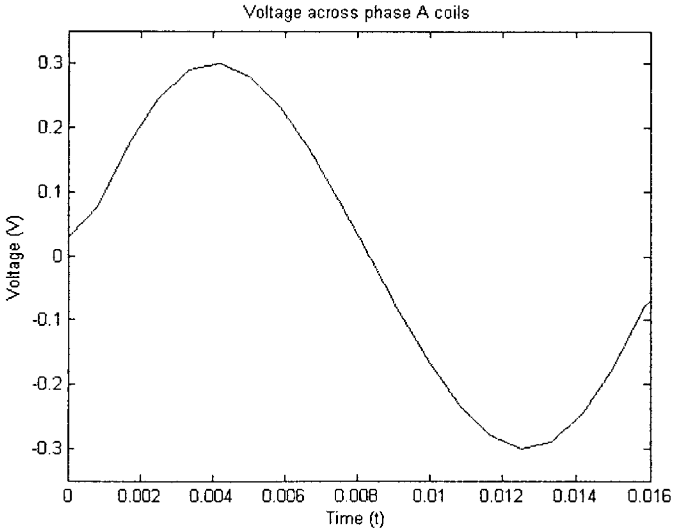

Figure 5-15: Voltage generated across phase A coils over a half a vibration cycle.

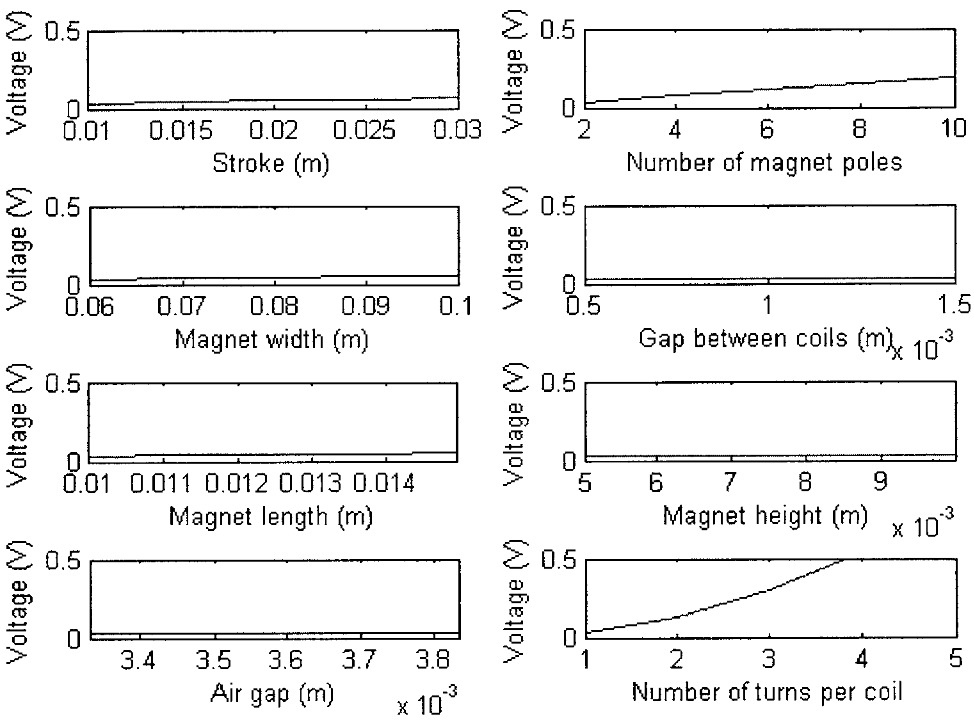

Figure 5-16: Sensitivity of the output voltage to system parameters.

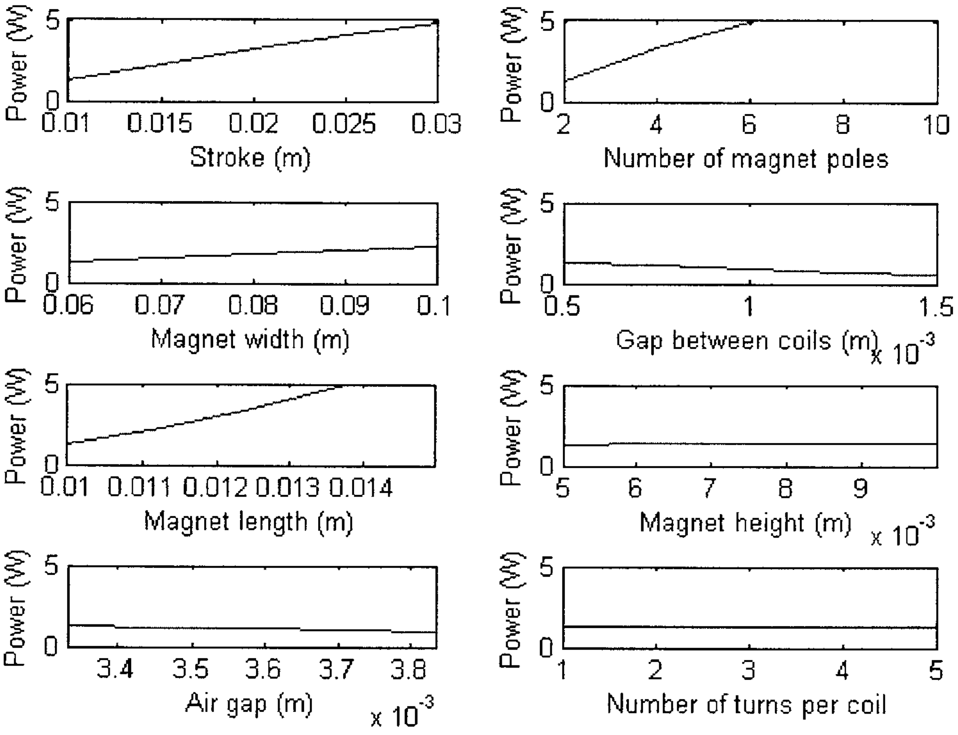

Figure 5-17: Sensitivity of the output power to system parameters.

Chapter 6

Experiments and Results

The power that can be extracted from a vibrating surface depends on the amplitude and frequency of the surface vibration (as discussed in section 4.1). Therefore, the feasibility of harvesting 0.53 W in a car door depends on the vibration profile of the car door surface. The first section of this chapter describes the collection of car door vibration data in order to determine the feasibility of harvesting the vibration energy to operate the windows.

The next two sections of the chapter respectively describe the magnet-through-coil and magnet-across coils systems that were built to test the MATLAB model predictions. The magnet-through-coil experiment involved dissecting a commercially available shaker flashlight and using its components to test the model predictions. The magnet-across-coils experiment involved building a prototype of a cantilever beam system for car-door energy harvesting application and testing it on a shaker table. The results of the experiments are also presented, and the discussions of the results follows in the next chapter.

6.1 Car Vibrations

Car vibration data under various driving conditions were collected to determine whether the energy in the vibrations is sufficient to operate the car windows via an energy harvester.

6.1.1 Low Frequency Vibration

The spectrum of car vibrations varies greatly with car model and driving conditions. In order to obtain an estimate of the order of magnitude of car vibrations, a single-axis accelerometer was used to measure the y-axis (up-and-down) vibrations in a car. The accelerometer was

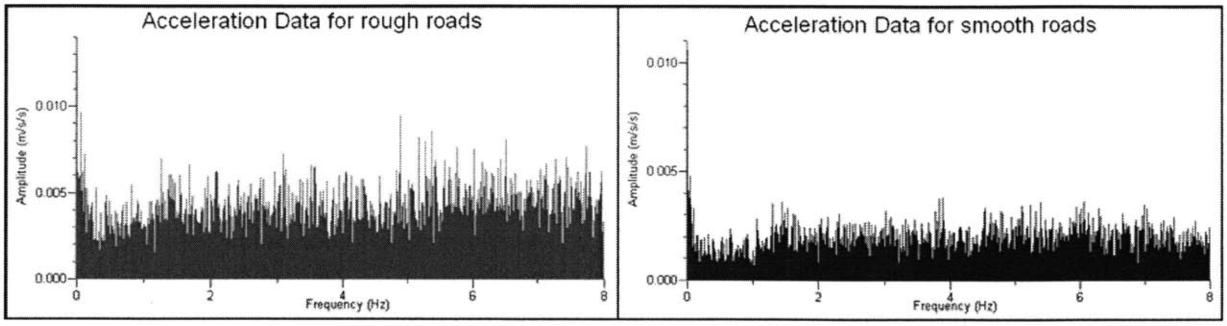

Figure 6-1: Frequency content of up-and-down vibrations in a car driving over rough and smooth roads in a city. The acceleration amplitude in $\frac{m}{s^2}$ is shown for a frequency range of $0 - 8\ Hz$.

taped to the window of the front passenger seat window and data was collected at a sampling rate of 1000 samples/minute, which is roughly 17 Hz. Data was collected for a time period of ten minutes each for two road conditions: rough roads and smooth roads. The acceleration data for driving over rough and smooth roads are given in Figure 6-1.

Analysis of the energy in the lower frequency vibrations indicated insufficient energy to provide power to car windows. Since the maximum power that can be extracted from mechanical vibrations depends on the frequency cubed (from Equation 4.11), vibration data were collected to analyze the feasibility of harvesting energy from higher frequency vibrations.

6.1.2 High Frequency Vibration

High frequency vibration data was collected by mounting a 3-axis accelerometer on the front passenger door of a Nissan Altima car. The accelerometer was epoxied to the car door panel so as to accurately measure the door vibrations. The accelerometer mounting is shown in Figure 6-2.

Data were collected under city driving conditions (with stop-and-go traffic) and at speeds of 55, 65 and 75 MPH. The data was collected in one-minute bursts at a sampling rate of 250 HZ. Figure 6-4 and 6-3 show the acceleration amplitude data for up-and-down and side-to-side vibrations in the Nissan Altima respectively for city driving conditions and at speeds of 55, 65 and 75 MPH.

The data show that side-to-side vibrations have more energy than up-and-down vibrations. Additionally, there is an vibration peak at approximately 30 Hz. This peak has very little correlation with driving conditions; the same peak is seen in the side-to-side vibration data for an idling car, as shown in Figure 6-5.

Figure 6-2: Placement of a three-axis accelerometer on a car door to collect vibration data.

Section 7.1 presents the data analysis and the discussion about the feasibility of car-door energy harvesting.

6.2 Magnet-through-coil Experiments

A NightStar® flashlight (Figure 6-6) was disassembled and used for the magnet-through-coil experiment. The magnet from the flashlight was attached to a rod driven by a Tamiya® motor. The magnet was then inserted into its original housing tube, while a single turn of wire was wrapped around the outer diameter of the housing tube. The motor was used to control the amplitude and frequency of the magnet's motion through the coil. A picture of the experimental setup is shown in Figure 6-7.

6.2.1 Single Turn of Wire

The voltage across the single turn of wire was measured first. The magnet was moved through the coil with a frequency of 1.5 Hz and amplitude of 3 cm. The resulting voltage waveform is shown in Figure 6-8. The data matched well with the model predictions, as demonstrated by Figure 6-9.

6.2.2 Coil of Wire

The experiment described in the previous section was repeated with a coil of wire instead of a single turn. The resulting voltage waveform is shown in Figure 6-10.

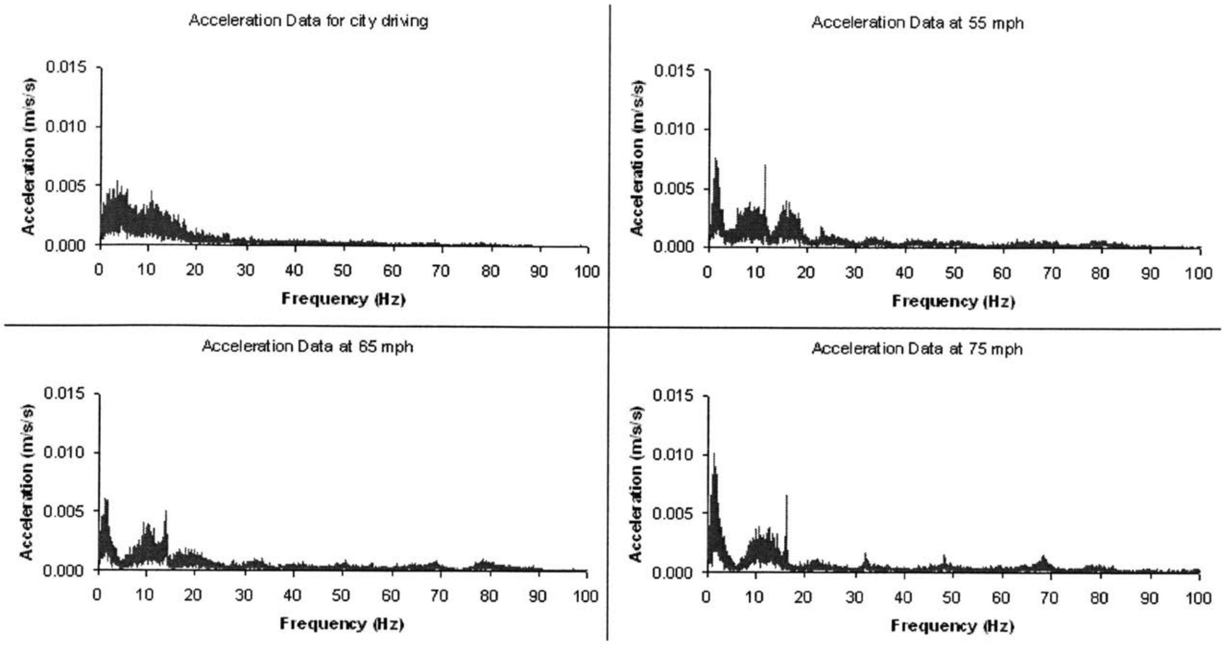

Figure 6-3: Acceleration data for up-and-down vibrations of a Nissan Altima car under various driving conditions.

Figure 6-11 shows an overlay of the predicted voltage and the real data for an offset of 1 cm between the magnet and coil. The waveforms are similar in frequency and peak voltage.

6.3 Magnet-across-coils Experiment

Four magnets were mounted on the end of a proof-mass on a cantilever beam. A single-phase coil (2 passes, 4 turns of wire) was taped onto a steel backing plate and the plate was attached to a block with a screw that allowed the distance between the magnets and coils to be varied. The system parameters have been listed in Tables 4.3 and 5.2, and drawings of the system parts are included in Appendix B. Figure 6-12 shows the cantilever beam with the magnetic induction system assembled. The system was shaken at 30 Hz with an input amplitude of 0.25 mm.

The distance between the magnets and the coils was varied and the peak output recorded for each case. Figure 6-13 shows an overlay of the data points from the experiments on the predicted curve from the MATLAB model.

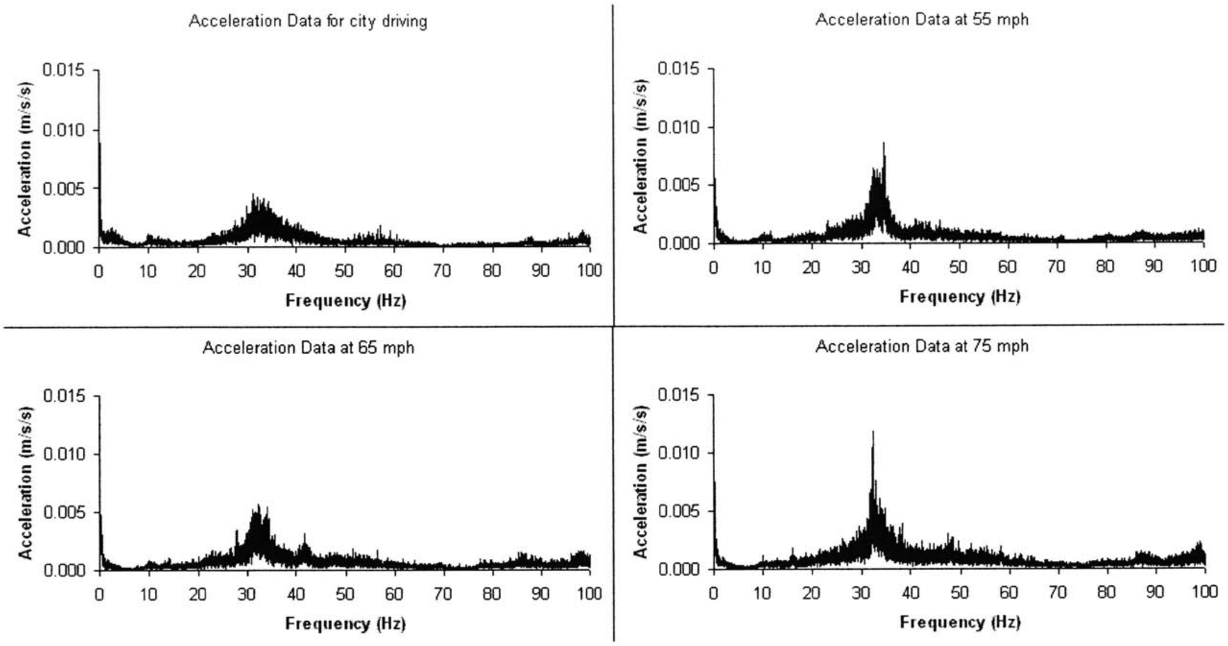

Figure 6-4: Acceleration data for side-to-side vibrations of a Nissan Altima car under various driving conditions.

6.4 Summary

This chapter described the collection of car vibration data and the results of testing the magnet-through-coil and magnet-across-coils systems. The next chapter discusses the implications of the results, the reasons for discrepancies from the predictions, and the scope for future work to build on the lessons learnt.

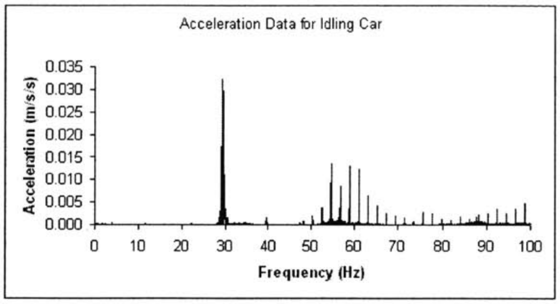

Figure 6-5: Acceleration data from side-to-side vibrations in a Nissan Altima car in idling condition.

Figure 6-6: NightStar®Flashlight before dissection.

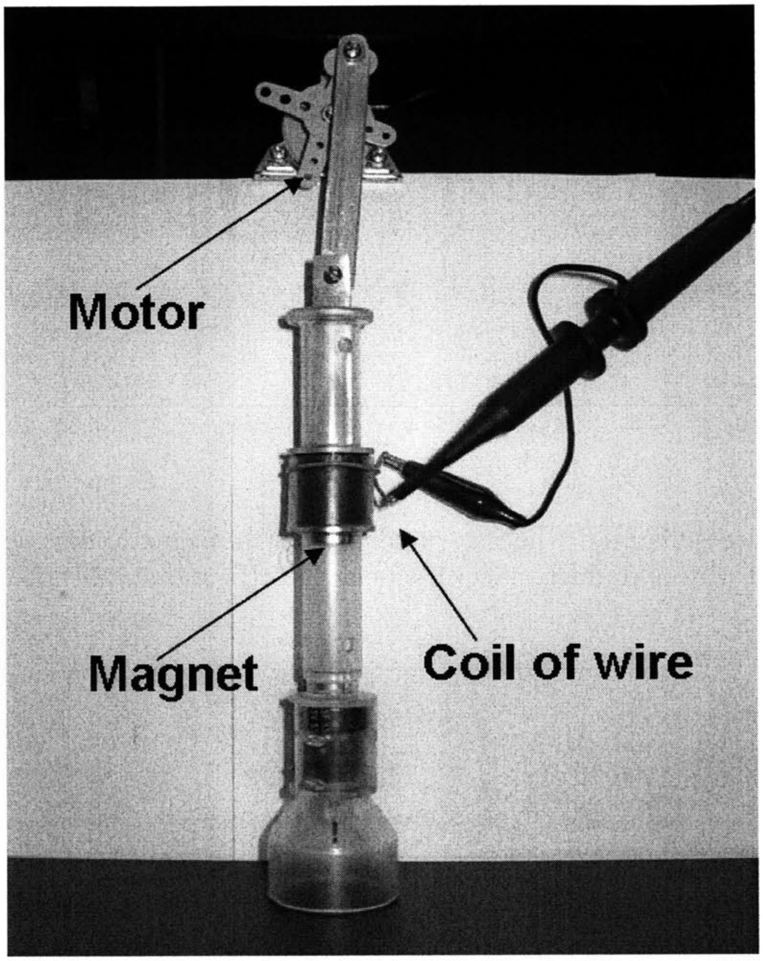

Figure 6-7: Experimental setup for voltage generation across a single turn of wire due to the movement of a magnet at a known frequency and amplitude.

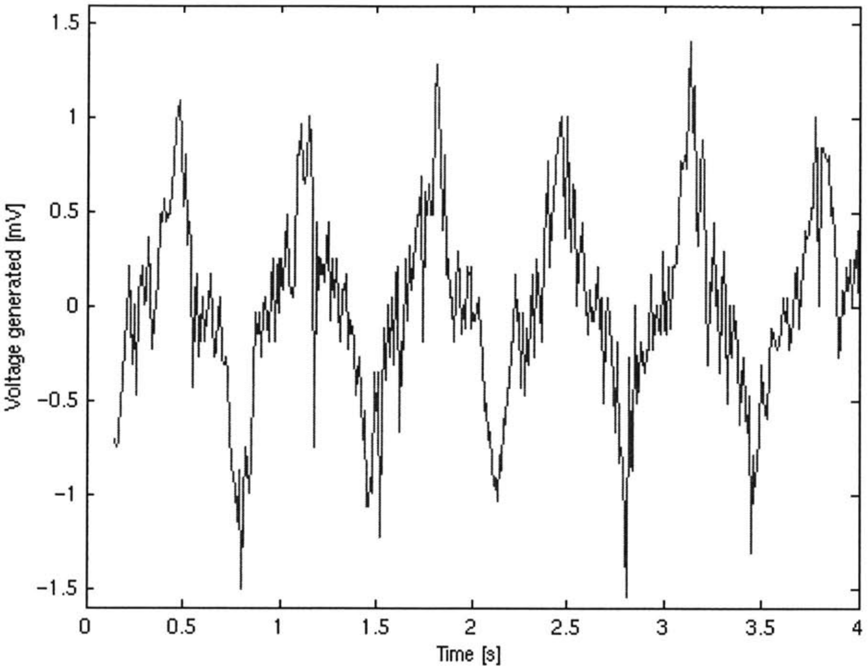

Figure 6-8: Voltage generated when a bar magnet with magnetic flux density 1.2 T moves through a turn of wire of diameter at a frequency 1.5 Hz and amplitude 3 cm.

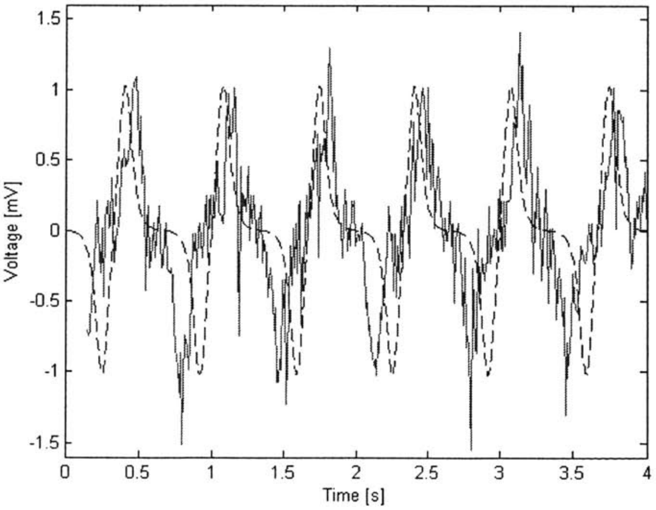

Figure 6-9: Overlay of predicted waveform (dashed line) and actual data (solid line) of the voltage generated when a bar magnet with magnetic flux density 1.2 T placed at ±1 cm moves through a turn of wire of diameter at a frequency 1.5 Hz and amplitude 3 cm.

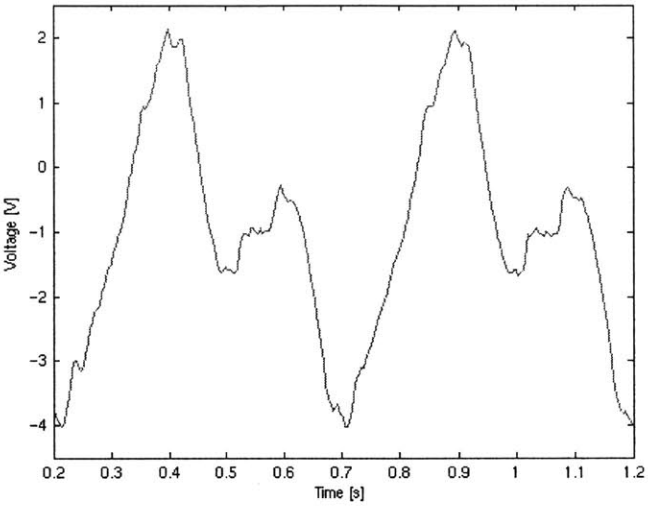

Figure 6-10: Voltage generated when a bar magnet with magnetic flux density 1.2 T moves at a frequency 1 Hz and amplitude 3 cm through a coil with 2,500 turns of wire, length 2 cm and average diameter 1 cm.

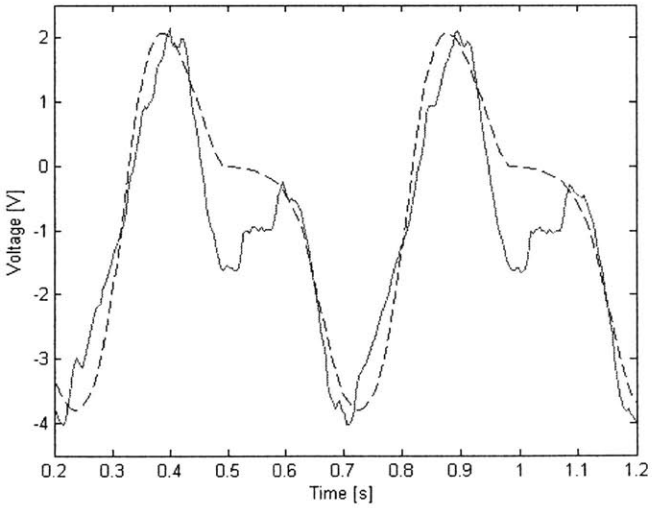

Figure 6-11: Overlay of predicted waveform (dashed line) and actual data (solid line) of the voltage generated when a bar magnet with poles of magnitude placed at ±1 cm moves at a frequency 1 Hz and amplitude 3 cm through a coil with 2,500 turns of wire, length 2 cm, and average diameter 1 cm.

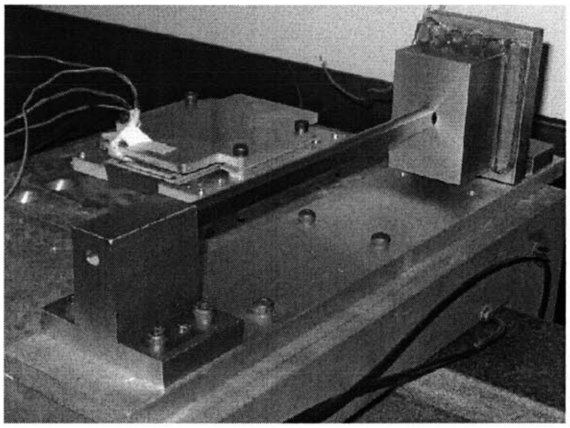

Figure 6-12: Experimental setup for voltage generation across a single phase coil (2 passes, 4 turns of wire) due to the movements at a fixed frequency and amplitude.

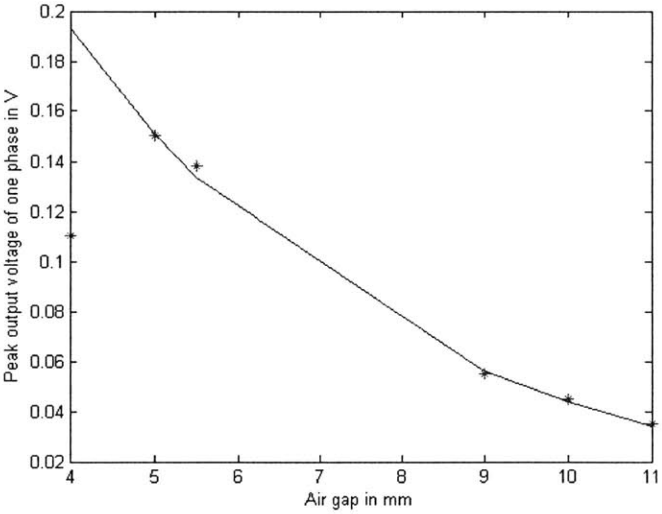

Figure 6-13: Overlay of predicted waveform (solid line) and experimental data points of the voltage generated across a single phase coil (2 passes, 4 turns of wire) as the air gap is varied from 4 to 11 mm. Four magnet poles move across the coil at a frequency of 30 Hz with a 3mm stroke.

Chapter 7

Discussion and Conclusions

The aim of this chapter is to summarize the lessons learnt through the work described in this thesis. The first section analyses the car door vibration data and discusses the feasibility of using energy harvesting to power car windows. The next section discusses the results from the experiments to test the MATLAB models of the magnetic induction systems, and attempts to explain discrepancies between the data and predictions. Each section includes recommendations for further work and improvement.

7.1 Car Vibration

The collection of car-door vibration data was described in Section 6.1; this section describes the data analysis and the conclusions about the feasibility of car-door energy harvesting to power car windows.

7.1.1 Data Analysis

The high-frequency car-door vibration data collected is surprising in many ways. Aspects that require explanation include:

1. Why do the side-to-side vibrations have the highest amplitude?
2. Why is the vibration peak frequency independent of driving conditions?
3. Why is the vibration amplitude not strongly correlated to car speed?

I believe that the answers to these questions lie in the car door geometry and accelerometer placement. The accelerometer was rigidly attached to the middle of the outside door panel. This panel, made of sheet metal, is anchored to the other car door panels along its edges. This means that the sheet forms a vibrating membrane with a certain resonance frequency. The relatively high amplitude of the side-to-side vibrations is explained by the fact that the vibrating sheet is most compliant in that direction, because of its low thickness.

Another important consequence of the panel geometry is that the vibrating sheet has a fixed resonance frequency. In the Nissan Altima car, the resonance frequency is close to 30 Hz. This explains why the peak vibration is always around the same frequency. It also accounts for the relative independence of the amplitude and car speed - all vibration input excites the resonance frequency to some extent. In the case of the idling car, the vibrations from the car engine cause the door panel to vibrate.

The presence of a fixed resonance frequency is very convenient from the energy harvesting point of view because a harvesting system can be built and optimized to operate at the door panel's resonance frequency.

The quantitative data analysis began with plotting the power in the vibrations as a function of frequency, to determine which frequency has the highest energy content. Equation 4.11 implied that the power in vibrations is a function of the frequency as well as the amplitude, and so we couldn't assume that the frequencies with highest amplitude had the most power. The power vs. vibration plots showed that the highest power was at the 30 Hz vibration peak.

The next step was to form an estimate of the energy that could be harvested from the car vibrations. At any given frequency the power that can be extracted is known; however, the energy harvesting system will not to be selective enough to only convert energy at one frequency. Therefore, the energy from vibrations along a 1 Hz band centered at the peak frequency were added, and the sum of the energy from all the frequencies was considered a reasonable estimate of the energy that can be harvested from the car door vibrations.

7.1.2 Energy Harvesting Feasibility

The vibration data indicates that there is sufficient energy in car vibrations to support the operation of a wireless window mechanism. For a vibrating mass of 1 kg, vibration frequency of 30 Hz (approximately 190 rad/s), input vibration amplitude from the data and relative vibration amplitude of 3 cm, the energy harvested over 5 minutes (300 seconds) will be:

$$City\ driving\ :\ P * t = 0.5 m\omega^3 yzt = 0.5 * 1 * 190^3 * 7.8 * 10^{-6} * 0.03 * 300 = 243\ J.$$

$$At\ 55\ mph: \ P*t = 0.5m\omega^3yzt = 0.5*1*190^3*1.4*10^{-5}*0.03*300 = 432\ J.$$

$$At\ 65\ mph: \ P*t = 0.5m\omega^3yzt = 0.5*1*190^3*9.0*10^{-6}*0.03*300 = 282\ J.$$

$$At\ 75\ mph: \ P*t = 0.5m\omega^3yzt = 0.5*1*190^3*1.7*10^{-5}*0.03*300 = 534\ J.$$

The efficient window design developed by Durand[1] requires approximately 160 joules per open-close cycle. The calculations show that driving for 5 minutes under various driving conditions will generate enough energy to power one window open-close cycle. These calculations are for a device that harvests energy from a 1 Hz band centered around the peak frequency; increasing this frequency range will enable even more energy to be harvested.

It is expected that there will be some losses from friction in the energy harvesting mechanism and from the electronics. Friction losses can be minimized by designing a flexure with the desired resonant frequency and thus eliminating bearing surfaces from the device. Similarly, careful design of the power electronics can minimize losses in that area. Even allowing for up to 30% losses from these sources, the 160 joules energy requirement is still met.

In conclusion, the car vibrations provide enough energy to make energy harvesting a feasible option for powering efficient window mechanisms.

We have proven that energy harvesting can be used in car doors; but should it be? The considerations in terms of added weight and cost to the car are more difficult. A vibrating mass of 1 kg, and approximately another 1 kg in coils, mounting parts and electronics will need to be added to each car door. It will only be worthwhile if additional cost, 8 kg of added weight, and the complexity of installing the energy harvesting system are compensated for by the reduction in wiring harness cost, weight and complexity in a car with 'wireless doors'; this is a determination for car manufacturers to make.

7.1.3 Recommendations for Future Work

Future work should include an iteration of the prototype to create a system that can be installed in a car door. The mounting parts of the prototype should be redesigned to meet weight constraints. A finite-element model of the car door should be analyzed to understand the dynamics of the door when the energy harvesting mechanism is mounted on it. This analysis would also help to determine the best point to attach the harvesting system to the car door.

---

[1] Keith Durand, MIT SM Thesis, June 2007

7.2 Magnetic Induction Systems

This section discusses the results from the magnet-through-coil and magnet-across-coils experiments. While the peak voltage produced across the coils matched extremely well with predictions in both cases, some discrepancies were observed in the detailed waveforms, and these are addressed. The section also provides suggestions for improvements to the MATLAB models as well as future experiments to help validate them.

7.2.1 Magnet-through-coil System

Figure 6-11 shows that the experimental data does not conform exactly to the prediction waveform for the voltage across the ends of a coil. The reason for the difference between the data and prediction waveform is probably due to the fact that the motor did not a produce a perfect single-frequency sinusoid as a function of time. The close matching of open-circuit voltage amplitude that the model is accurate for peak voltage predictions.

7.2.2 Magnet-across-coils System

The test setup for the magnet-across-coils system was less than optimal. It was clear that the table was not shaking with a fixed amplitude and single frequency. The control system for the shaker table was unreliable – for example, the command to increase the table vibration amplitude from 0.25 mm to 0.5 mm resulted in a decrease in the table amplitude. It was not clear whether this was because the control system was providing incorrect input to the actuators or because the system had reached its operating capacity. There was also a lot of noise in the voltage output signal. Some of the noise was reduced by low-pass-filtering the output with a capacitor, but the signal was still fuzzy and the amplitude was not uniform.

Despite these issues, the maximum open-circuit voltage (occurring at the point of highest amplitude) matched the model predictions. The data point for the gap = 4 mm (Figure 6-13) was considerably lower than expected, but this was later explained by the magnet being close enough to rub against the coils, adding unexpected friction to the system.

7.2.3 Recommendations for Future Work

The magnet-through-coil experiment should be repeated with a sinusoidal displacement input to check for the source of discrepancy between the predictions and data waveform shapes.

The magnet-across-coils experiment should be repeated on a shaker table with more deterministic output. In addition, the position of the magnets should be mapped independently to decouple the analysis of (1) the vibration of the magnets resulting from the vibration of the table, and (2) the voltage across the coils due to the vibration of the magnets. Finally, once the model has been completely validated for a one-phase coil, tests should be conducted to test the predictions for a three-phase coil.

The MATLAB models for both systems can be extended to enable the prediction of the response of the systems to a random waveform as opposed to a fixed-amplitude single frequency sinusoidal input. This will increase their utility as design and analysis tools.

Appendix A

MATLAB Code

A.1 Magnet-though-coil Code

```
 clear all

%-------------- Inputs -----------

% Constants

mu0 = pi*4e-7; % N/(A^2)

% Magnet parameters

Br  = 1.2;      % T (N/(Am))    magnetization flux density
r_m = 6.35e-3; % m             magnet radius
l_m = 1.9e-2; % m             coil radius

% Coil parameters

N    = 3500; % turns
d_max= 1.8e-2;  % m            maximum diameter
d_min= 1.3e-2; % m            minimum diameter
l_c  = 1.9e-2; % m            length of coil
R0   = 0.351; % ohm/m         coil resistivity
```

```
% Vibration parameters

f      = 1.02;       % Hz      Vibration frequency
a      = 3e-2;        % m       Vibration amplitude
offset = -1e-2;       % m       Coil offset

%---------- End Inputs ----------


% Coil parameters

N0   = N/l_c;           % turns/m
d_c  = (d_max+d_min)/2; % m         coil average diameter
A_c  = pi*(d_c^2)/4; % m^2       coil cross-sectional area

R    = N*pi*d_c*R0;     % ohms      coil resistance
L    = mu0*N*N*A_c/l_c; % H (Nm/(A^2))  coil inductance

if (R/(2*pi*f*L)<50)   % check that coil resistance dominates
    disp('Warning: coil inductance not negligible')
end

h_min = offset-l_c/2 -a;  %m    lowest point of coil travel
h_max = offset-l_c/2 +a;  %m    highest point of coil travel

% magnetic flux through coil

dh       = (h_max - h_min)/100;                    %m
h        = [h_min-2*dh:dh:(h_max+l_c)+2*dh];   %m
q_m      = Br*pi*r_m*r_m;
r_c      = d_c/2;

% calculation of H_m
```

```
phi1 = -sign(-l_m/2.+h)*q_m.*(sqrt(r_c^2+((-l_m/2.+h).*(-l_m/2.+h)))
       -abs(-l_m/2.+h))./(2*sqrt(r_c^2+(-l_m/2.+h).*(-l_m/2.+h)));
phi2 = sign(l_m/2.+h)*q_m.*(sqrt(r_c^2+((l_m/2.+h).*(l_m/2.+h)))
       -abs(l_m/2.+h))./(2*sqrt(r_c^2+(l_m/2.+h).*(l_m/2.+h)));

% total H_m
phi = phi1 + phi2;

y = 0.0075;
phi0 = [phi(2:length(phi)) 2*phi(length(phi))-phi(length(phi)-1)];
dphidh = (phi0-phi)/dh;
dphidhs = dphidh;
dphidhs(69) = 0.5*(dphidhs(68)+dphidhs(70));
dphidhs(101) = 0.5*(dphidhs(100)+dphidhs(102));

% sum flux through coil during travel
h_travel = [h_min:dh:h_max];
Phi = zeros(1,length(h_travel));
dPhidh = zeros(1,length(h_travel));
for x = 1:length(h_travel)
y = x;
P = 0;
    dP= 0;
while (h(y) < (h_travel(x)+l_c) )
        P = P + N0*dh*phi(y);
        dP= dP+ N0*dh*dphidhs(y);
y=y+1;
    end
    Phi(x)    = P;  % total Phi through the coil when lower end is at h(x)
    dPhidhs(x) = dP;% total dPhidh through the coil when lower end is at h(x).
end

dPhidhms = [dPhidhs -dPhidhs dPhidhs -dPhidhs dPhidhs
           -dPhidhs dPhidhs -dPhidhs dPhidhs -dPhidhs];
```

```
dt  = (5/f)/(length(dPhidhms)-1);

t   = [0:dt:10/(2*f)];          % s         time
x   = a*cos(2*pi*f.*t);         % m         position
v   = a*2*pi*f*sin(2*pi*f.*t);  % m/s       velocity

V_s = dPhidhms.*v;              % V         Voltage across coil!
```

A.2 Magnet-across-coils Code

```
clear all

%-------------- Inputs -----------

% Vibration parameters
f = 30;             % in Hz, vibration frequency
a = 3e-3;           % in m, vibration amplitude

% Geometry parameters
np = 4;              % number of magnets (poles)
d = .0e-3;           % in m, half the gap between magnets
l = 0.5*.0254;       % in m, length of each magnet (pole)
w = 3*.0254;         % in m, width (into the paper)
x_A = 0.25*.0254;    % in m, height of magnets
x_B = 4e-3;          % in m, height of air gap

% Magnet parameters
s_max = 1.31;        % in T (Wb/m2), Maximum charge density; equal to Br
mu_0 = pi*4e-7;      % in Wb/(A.m), Magnetic permeability of vacuum

% Coil parameters
```

```
i = 1;              % in A, Current through coils
t = .08/3*.0254;    % in m, spacing between coils
    g = (((l+2*d)/3)-t)/2; % half a coil length
wd = 0.8128e-3;     % in m, diameter of the wire
nc = 2;             % number of coils (per phase)
nt = 4;             % number of turns per coil
R0 = 16.78e-9;      % in ohm.m, resistivity of copper

% Fourier sum parameters
N = 50;             % Number of terms added in the fourier sum
res = 200;          % number of points per co-ordinate array

%-------------- End Inputs -----------

% Geometry
x_step = (x_A+x_B)/res;
z_step = (np*(2*d+l))/res;

x = [-x_B:x_step:x_A];
x = repmat(x,res+1,1);
z = [0:z_step:np*(2*d+l)];
z = repmat(z,res+1,1); z=z';
coil = floor(length(z)*(2*d+l)/(np*(2*d+l)));

% Loop to calculate fourier coefficients and magnetic potential constants
for p = 1:N
    k = 2*p-1; % even coefficients are 0, only calculate for odd values
    w_m = pi*k/(2*d+l);
    w_c = pi*k/(3*(2*g+t));
    b_m(p) = (4*s_max/k/pi)*cos((k*pi*d)/(l+2*d));
           % in T, magnets charge density fourier coefficients
    a_c(p) = (4*i/g/k/pi)*sin((k*pi*g)/(3*(2*g+t)));
           % in A/m, coils tangential magnetic field fourier coefficients
    A(p) = (b_m(p)*sinh(w_m*x_B))/(w_m*mu_0*sinh(w_m*(x_A+x_B)));
```

```
        % in A, constants for psi_A calculation
    C(p) = (-b_m(p)*sinh(w_m*x_A))/(w_m*mu_0*sinh(w_m*(x_A+x_B)));
        % in A, constants for psi_B calculation
    D(p) = a_c(p)/(w_c*sinh(w_c*(x_A+x_B)));
            % in A, constants for psi calculation
end

sigma = 0*z;                            % magnets charge density
Hz = 0*z;                               % coils tangential field at -x_B
psi_A = zeros(length(x),length(z));
      % magnetic potential in region A due to magnets
psi_B = zeros(length(x),length(z));
      % magnetic potential in region B due to magnets
psi_c_A = zeros(length(x),length(z));
        % magnetic potential due to coils, phase A

for i = 1:N         % loop to sum the fourier series terms
    j = 2*i-1;
 sigma = sigma + b_m(i).*sin(z.*(j*pi/(l+2*d)));
       % in T, magnets charge density
 psi_A = psi_A + A(i)*sinh(pi*j.*(x-x_A)/(l+2*d)).*sin(z.*(pi*j/(l+2*d)));
       % in A, magnetic potential in region A due to magnets
 psi_B = psi_B + C(i)*sinh(pi*j.*(x+x_B)/(l+2*d)).*sin(z.*(pi*j/(l+2*d)));
       % in A, magnetic potential in region B due to magnets
 Hz = Hz + a_c(i).*cos(z.*(j*pi/(3*(2*g+t))));
    % in A/m, coils tangential field at x_B
 psi_c_A = psi_c_A+D(i)*sinh(pi*j.*(x-x_A)/(3*(2*g+t)))
           .*sin(z.*(j*pi/(3*(2*g+t))));
        % in A, magnetic potential due to coils
end

m1 = ceil(length(x)*x_B/(x_A+x_B));
m2 = floor(length(x)*x_B/(x_A+x_B));
psi_A(:,1:m2) = 0;          % zeroing out Region B where psi_A is invalid
```

```
psi_B(:,m1:length(z)) = 0;  % zeroing out Region A where psi_B is invalid
psi_m = psi_A + psi_B;


[Hm_x,Hm_z] = gradient(psi_m,x_step,z_step);
            % in A/m, H in x and z due to magnets
[Hc_A_x,Hc_A_z] = gradient(psi_c_A,x_step,z_step);
                % in A/m, H in x and z due to coils, phase A

if (a>l)    m3 = ceil((a-l)/z_step);
else        m3 = 0;
end

Hm_x_surf = Hm_x(:,1); %Values of Hm_x at the coils surface
HcA_x_surf = Hc_A_x(:,1); HcA_x_surf = [HcA_x_surf' zeros(1,m3)];
           % Values of Hc_A_x at the coils surface

newres = 21; % number of points in position vector for given amplitude
time = [0:1/(2*f*(newres-1)):1/(2*f)];    % in s, time for a half-cycle
omega = 2*pi*f;                           % in rad/s, vibration frequency
pos = a*sin(omega*time);                  % in m, position
vel = a*omega*cos(omega*time);            % in m/s, velocity

L = zeros(1,newres);
lambda = zeros(1,length(time));
for q = 1:length(time)
        Lstep = z_step*cumsum(HcA_x_surf(q:q+coil));
      % Sum of H_c_x over area of an A coil, for one magnet stroke
        q1 = 1+floor((pos(q)/z_step)); q2 = 1+ceil((pos(q)/z_step));
        lamstepA1 = z_step*cumsum(Hm_x_surf(q1:q1+coil));
      % Sum of H_m_x over area of an A coil, for one magnet stroke
        lamstepA2 = z_step*cumsum(Hm_x_surf(q2:q2+coil));
 if q1==q2
  lamstepA = lamstepA1;
```

```
 else
  lamstepA = lamstepA1+(lamstepA2-lamstepA1)*(pos(q)-z(q1))/(z(q2)-z(q1));
 end
        L(q)= Lstep(coil); % Self-inductance of one phase of the coil
        lambda_A(q) = nc*nt*mu_0*lamstepA(coil)*(np/2)*w;
              % magnetic flux through phase A
end

L = max(L);
  R = R0*(nc*nt*np*(w+l))/(pi*wd^2/4);    % Resistance of the coil wire
if (R/(2*pi*f*L)<50)    % check that coil resistance dominates
    disp('Warning: coil inductance not negligible')
end

V_A = gradient(lambda_A,time);  % Voltage across phase A!
Vmax_A = max(V_A);              % Peak voltage

R_l = R;                % load resistance set equal to the coil resistance
power_A = V_A.^2/(R_l); % in W, power dissipated in load resistance!
```

Appendix B

Part Drawings

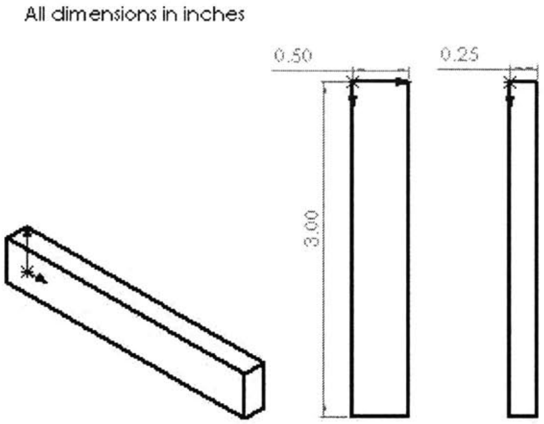

Figure B-1: Dimensions of the magnets used in the magnet-across-coils system.

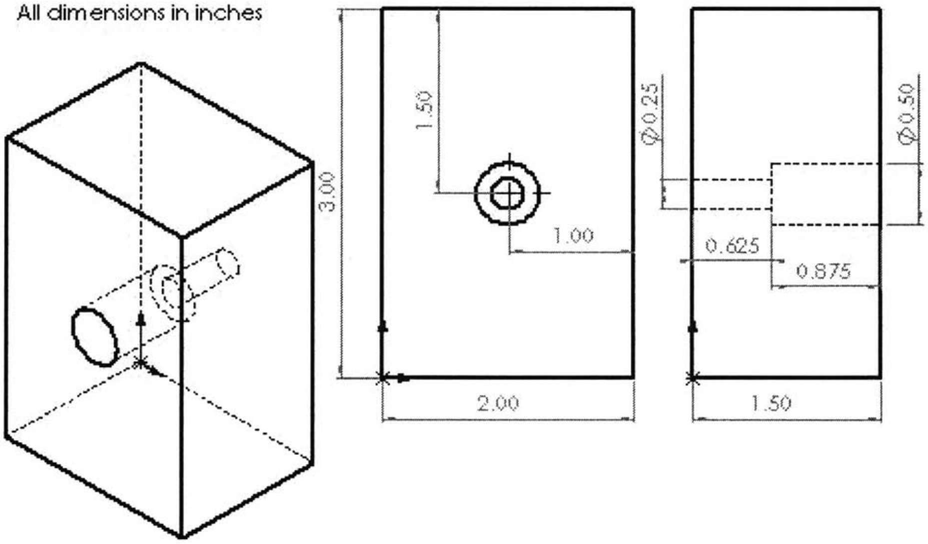

Figure B-2: Dimensions of the backing plate for the magnets used in the magnet-across-coils system.

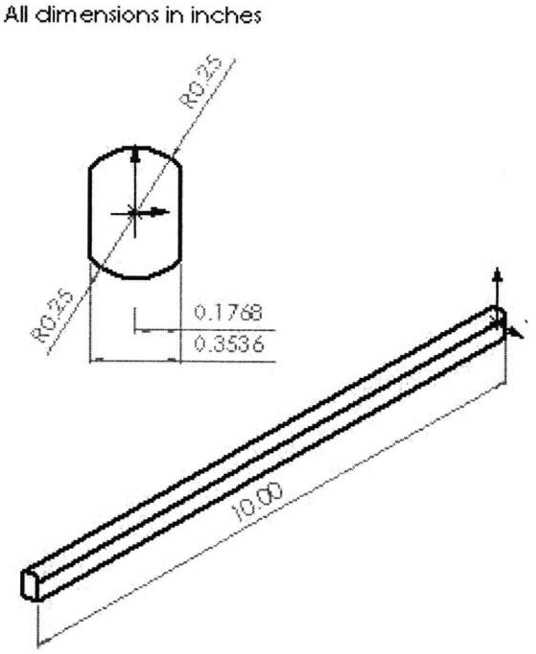

Figure B-3: Dimensions of the centilever beam used in the magnet-across-coils system.

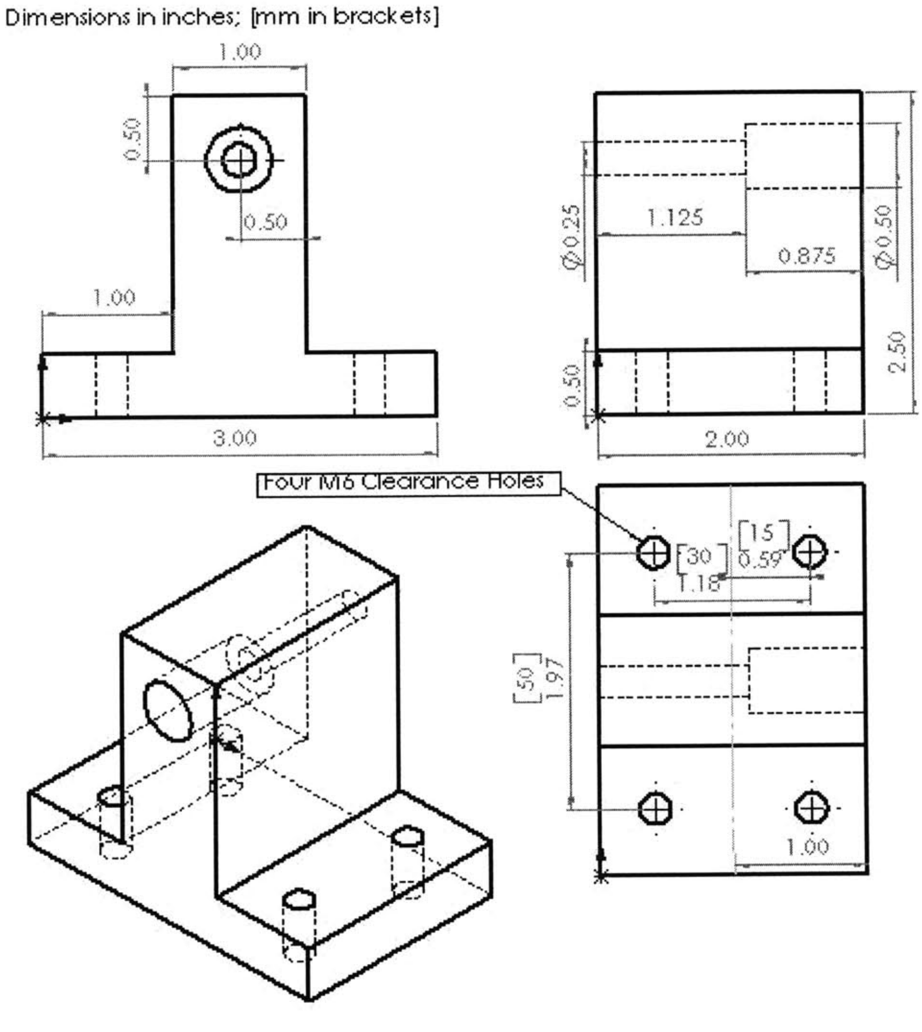

Figure B-4: Dimensions of the mount for the cantilever beam used in the magnet-across-coils system.

All dimensions in inches

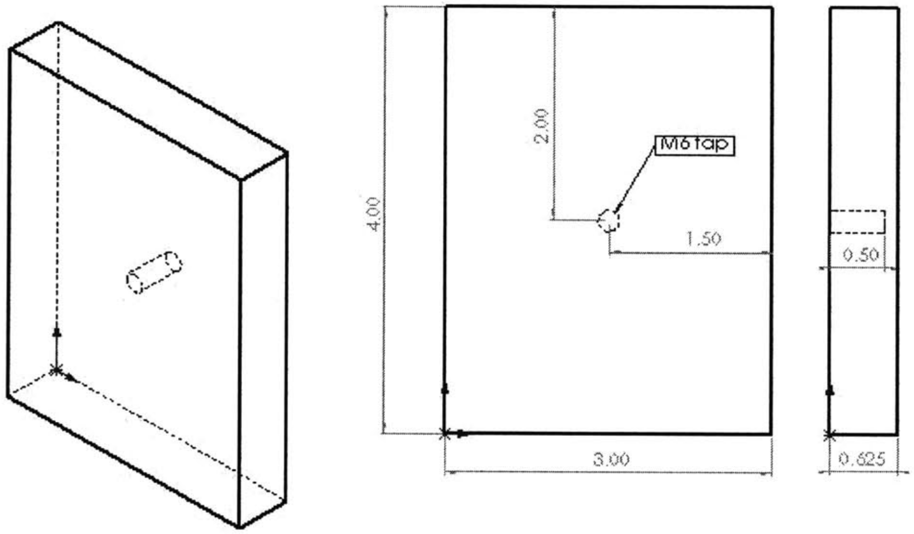

Figure B-5: Dimensions of the backing plate for the magnet-across-coils system coils.

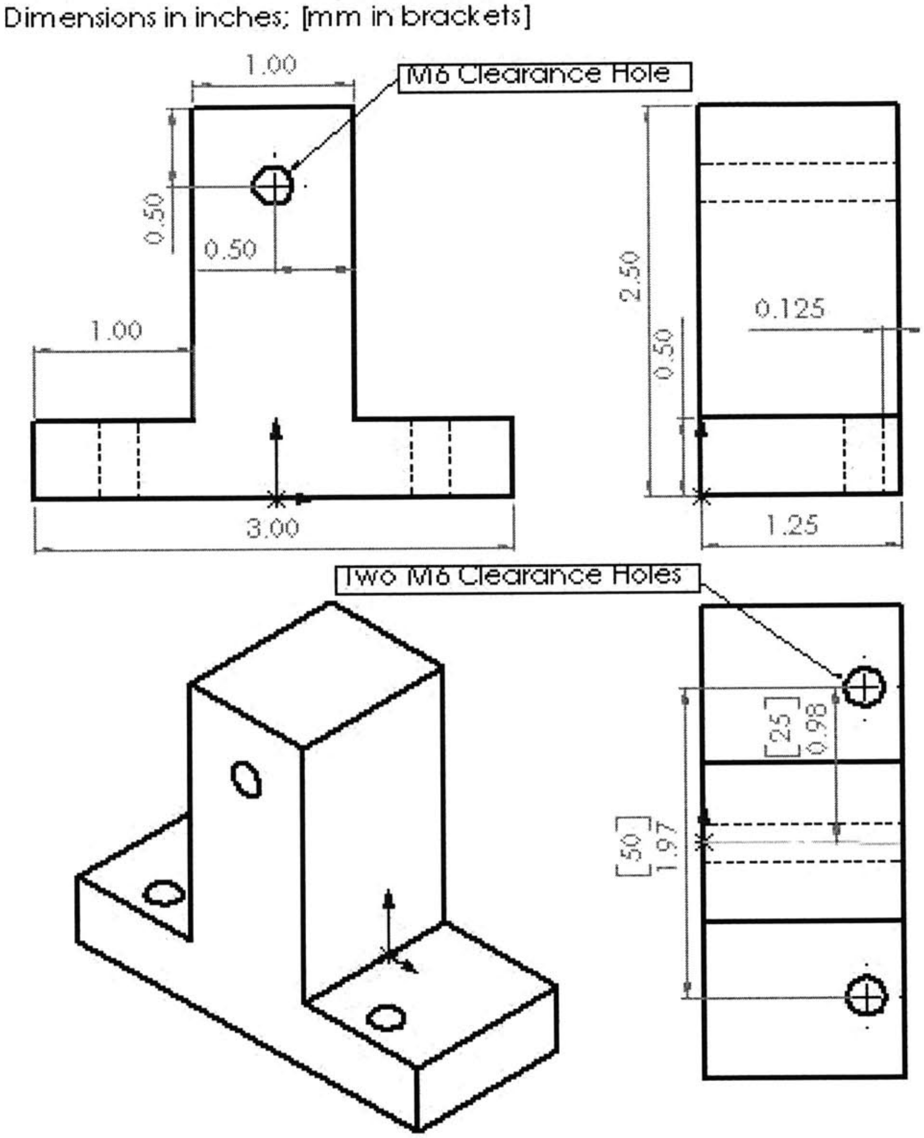

Figure B-6: Dimensions of the mount for the backing plate of the magnet-across-coils system coils.

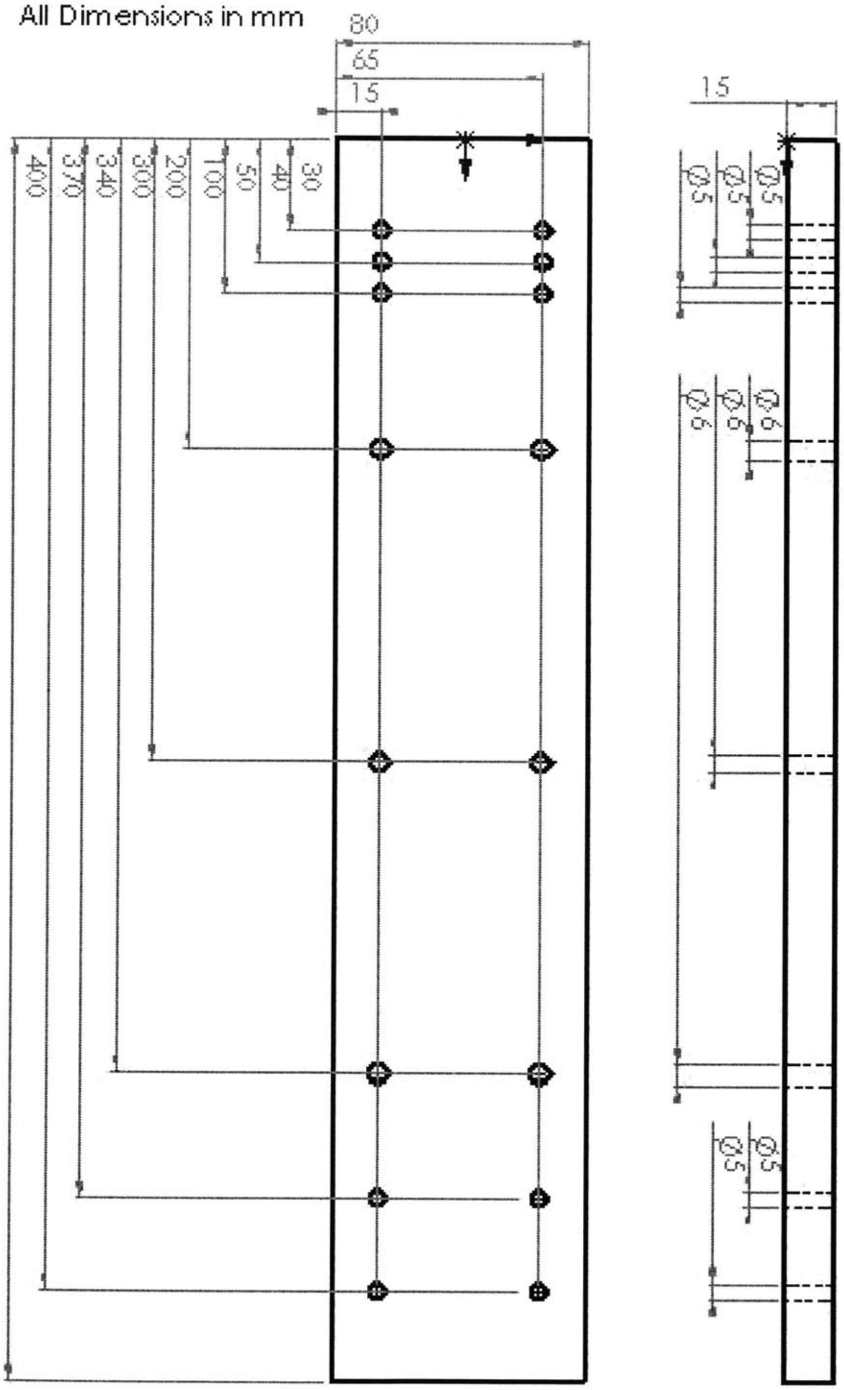

Figure B-7: Dimensions of the baseplate of the magnet-across-coils system.

Appendix C

Fourier Series Coefficient Calculations

A function $f(z)$ that is periodic with period Z can be expressed as a Fourier series of general form

$$f(z) = a_0 + \sum_{k=1}^{\infty}[a_k \cos(\frac{2\pi kz}{Z}) + b_k \sin(\frac{2\pi kz}{Z})],$$

with Fourier coefficients a_0, a_k and b_k. The formulae for the calculation of Fourier coefficients are:

$$a_0 = \frac{1}{Z}\int_0^Z f(z)dz.$$

$$a_k = \frac{2}{Z}\int_0^Z f(z)\cos(\frac{2\pi kz}{Z})dz.$$

$$b_k = \frac{2}{Z}\int_0^Z f(z)\sin(\frac{2\pi kz}{Z})dz.$$

C.1 Magnetic Charge Density at Plane $x = 0$

The magnetic charge density waveform, σ_M, at plane $x = 0$, due to the magnets, can be represented by

$$\sigma_M = a_0 + \sum_{k=1}^{\infty}[a_k \cos(\frac{2\pi kz}{Z}) + b_k \sin(\frac{2\pi kz}{Z})],$$

where Z, the spatial period of the magnetic charge density function, is $2(l + 2d)$. Since the charge density function is odd and unbiased, the cosine components of the Fourier sum will be zero ($a_0 = a_k = 0$). The detailed Fourier coefficient calculations are:

$$a_0 = \frac{1}{2(l+2d)}\Big[\int_d^{l+d} \sigma_{max} dz + \int_{l+3d}^{2l+3d} -\sigma_{max} dz\Big].$$

$$a_0 = \frac{\sigma_{max}}{2(l+2d)}\Big[z\Big|_d^{l+d} - z\Big|_{l+3d}^{2l+3d}\Big] = \frac{\sigma_{max}}{2(l+2d)}\Big[(l+d) - d - (2l+3d) + (l+3d)\Big].$$

$$a_0 = 0.$$

$$a_k = \frac{2}{2(l+2d)}\Big[\int_d^{l+d} \sigma_{max} \cos\Big(\frac{2\pi k z}{2(l+2d)}\Big) dz + \int_{l+3d}^{2l+3d} -\sigma_{max} \cos\Big(\frac{2\pi k z}{2(l+2d)}\Big) dz\Big].$$

$$a_k = \frac{\sigma_{max}}{k\pi}\Big[\sin\Big(\frac{\pi k z}{l+2d}\Big)\Big|_d^{l+d} - \sin\Big(\frac{\pi k z}{l+2d}\Big)\Big|_{l+3d}^{2l+3d}\Big].$$

$$a_k = \frac{\sigma_{max}}{k\pi}\Big[\sin\Big(\frac{\pi k(l+d)}{l+2d}\Big) - \sin\Big(\frac{\pi k d}{l+2d}\Big) - \sin\Big(\frac{\pi k(2l+3d)}{l+2d}\Big) + \sin\Big(\frac{\pi k(l+3d)}{l+2d}\Big)\Big].$$

$$a_k = \frac{\sigma_{max}}{k\pi}\Big[\sin\Big(k\pi - \frac{\pi k d}{l+2d}\Big) - \sin\Big(\frac{\pi k d}{l+2d}\Big) - \sin\Big(\frac{-\pi k d}{l+2d} + 2k\pi\Big) + \sin\Big(\frac{\pi k d}{l+2d} + k\pi\Big)\Big].$$

$$a_k = 0.$$

$$b_k = \frac{2}{2(l+2d)}\Big[\int_d^{l+d} \sigma_{max} \sin\Big(\frac{2\pi k z}{2(l+2d)}\Big) dz + \int_{l+3d}^{2l+3d} -\sigma_{max} \sin\Big(\frac{2\pi k z}{2(l+2d)}\Big) dz\Big].$$

$$b_k = \frac{\sigma_{max}}{k\pi}\Big[-\cos\Big(\frac{\pi k z}{l+2d}\Big)\Big|_d^{l+d} + \cos\Big(\frac{\pi k z}{l+2d}\Big)\Big|_{l+3d}^{2l+3d}\Big].$$

$$b_k = \frac{\sigma_{max}}{k\pi}\Big[-\cos\Big(\frac{\pi k(l+d)}{l+2d}\Big) + \cos\Big(\frac{\pi k d}{l+2d}\Big) + \cos\Big(\frac{\pi k(2l+3d)}{l+2d}\Big) - \cos\Big(\frac{\pi k(l+3d)}{l+2d}\Big)\Big].$$

$$b_k = \frac{\sigma_{max}}{k\pi}\Big[-\cos\Big(k\pi - \frac{\pi k d}{l+2d}\Big) + \cos\Big(\frac{\pi k d}{l+2d}\Big) + \cos\Big(\frac{-\pi k d}{l+2d} + 2k\pi\Big) - \cos\Big(\frac{\pi k d}{l+2d} + k\pi\Big)\Big].$$

$$b_k = \begin{cases} \frac{4\sigma_{max}}{k\pi}\cos\Big(\frac{\pi k d}{l+2d}\Big) & \text{for odd } k. \\ 0 & \text{for even } k. \end{cases}$$

C.2 Tangential Magnetic Field at Plane $x = -x_B$

The tangential magnetic field, H_z, at plane $x = -x_B$, due to the current i passing through the phase A coils, can be expressed as

$$H_z = a_0 + \sum_{k=1}^{\infty}[a_k \cos(\frac{2\pi kz}{Z}) + b_k \sin(\frac{2\pi kz}{Z})],$$

where Z, the spatial period of the tangential magnetic field function, is $6(2g+t)$. Since the H_z waveform is even and unbiased, the contributions from sines will be zero. The Fourier coefficient calculations are:

$$a_0 = \frac{1}{6(2g+t)}\Big[\int_0^g \frac{i}{g}dz + \int_{5g+3t}^{7g+3t} \frac{-i}{g}dz + \int_{11g+6t}^{12g+6t)} \frac{i}{g}dz\Big].$$

$$a_0 = \frac{i}{6g(2g+t)}\Big[z\Big|_0^g - z\Big|_{5g+3t}^{7g+3t} + z\Big|_{11g+6t}^{12g+6t}\Big] = \frac{i}{6g(2g+t)}\big[g-(7g+3t)+(5g+3t)+(12g+6t)-(11g+6t)\big].$$

$$a_0 = 0.$$

$$a_k = \frac{2}{6(2g+t)}\Big[\int_0^g \frac{i}{g}\cos\Big(\frac{2\pi kz}{6(2g+t)}\Big)dz + \int_{5g+3t}^{7g+3t} \frac{-i}{g}\cos\Big(\frac{2\pi kz}{6(2g+t)}\Big)dz + \int_{11g+6t}^{12g+6t)} \frac{i}{g}\cos\Big(\frac{2\pi kz}{6(2g+t)}\Big)dz\Big].$$

$$a_k = \frac{i}{gk\pi}\Big[\sin\Big(\frac{\pi kz}{3(2g+t)}\Big)\Big|_0^g - \sin\Big(\frac{\pi kz}{3(2g+t)}\Big)\Big|_{5g+3t}^{7g+3t} + \sin\Big(\frac{\pi kz}{3(2g+t)}\Big)\Big|_{11g+6t}^{12g+6t}\Big].$$

$$a_k = \frac{i}{gk\pi}\Big[\sin\Big(\frac{\pi kg}{3(2g+t)}\Big) - \sin\Big(\frac{\pi k(7g+3t)}{3(2g+t)}\Big) + \sin\Big(\frac{\pi k(5g+3t)}{3(2g+t)}\Big) - \sin\Big(\frac{\pi k(11g+6t)}{3(2g+t)}\Big)\Big].$$

$$a_k = \frac{i}{gk\pi}\Big[\sin\Big(\frac{\pi kg}{3(2g+t)}\Big) - \sin\Big(k\pi + \frac{\pi kg}{3(2g+t)}\Big) + \sin\Big(k\pi - \frac{\pi kg}{3(2g+t)}\Big) - \sin\Big(2\pi k - \frac{\pi kg}{3(2g+t)}\Big)\Big].$$

$$a_k = \begin{cases} \frac{4i}{gk\pi}\sin\Big(\frac{\pi kg}{3(2t+g)}\Big) & \text{for odd } k. \\ 0 & \text{for even } k. \end{cases}$$

$$b_k = \frac{2}{6(2g+t)}\Big[\int_0^g \frac{i}{g}\sin\Big(\frac{2\pi kz}{6(2g+t)}\Big)dz + \int_{5g+3t}^{7g+3t} \frac{-i}{g}\sin\Big(\frac{2\pi kz}{6(2g+t)}\Big)dz + \int_{11g+6t}^{12g+6t)} \frac{i}{g}\sin\Big(\frac{2\pi kz}{6(2g+t)}\Big)dz\Big].$$

$$b_k = \frac{i}{gk\pi}\Big[-\cos\Big(\frac{\pi kz}{3(2g+t)}\Big)\Big|_0^g + \cos\Big(\frac{\pi kz}{3(2g+t)}\Big)\Big|_{5g+3t}^{7g+3t} - \cos\Big(\frac{\pi kz}{3(2g+t)}\Big)\Big|_{11g+6t}^{12g+6t}\Big].$$

$$b_k = \frac{i}{gk\pi}\Big[-\cos\Big(\frac{\pi kg}{3(2g+t)}\Big)+1+\cos\Big(\frac{\pi k(7g+3t)}{3(2g+t)}\Big)-\cos\Big(\frac{\pi k(5g+3t)}{3(2g+t)}\Big)-1+\cos\Big(\frac{\pi k(11g+6t)}{3(2g+t)}\Big)\Big].$$

$$b_k = \frac{i}{gk\pi}\Big[-\cos\Big(\frac{\pi kg}{3(2g+t)}\Big)+\cos\Big(k\pi+\frac{\pi kg}{3(2g+t)}\Big)-\cos\Big(k\pi-\frac{\pi kg}{3(2g+t)}\Big)+\cos\Big(2\pi k-\frac{\pi kg}{3(2g+t)}\Big)\Big].$$

$$b_k = 0.$$